

COVID-19 virtual patient cohort reveals immune mechanisms driving disease outcomes

Adrienne L. Jenner^{1,2}, Rosemary A. Aogo³, Sofia Alfonso⁴, Vivienne Crowe⁵, Amanda P. Smith³,
Penelope A. Morel⁶, Courtney L. Davis⁷ [¶], Amber M. Smith^{3¶}, Morgan Craig^{1,2, 4*¶}

¹CHU Sainte-Justine Research Centre, Montréal, Québec, Canada

²Department of Mathematics and Statistics, Université de Montréal, Montréal, Québec, Canada

³Department of Pediatrics, University of Tennessee Health Science Center, Memphis, Tennessee, USA

⁴Department of Physiology, McGill University, Montréal, Québec, Canada

⁵Department of Mathematics and Statistics, Concordia University, Montréal, Québec, Canada

⁶Department of Immunology, University of Pittsburgh, Pittsburgh, Pennsylvania, USA

⁷Natural Science Division, Pepperdine University, Malibu, California, USA

[¶]Co-senior authors

*Corresponding author: morgan.craig@umontreal.ca

38 **Abstract**

39 To understand the diversity of immune responses to SARS-CoV-2 and distinguish features that
40 predispose individuals to severe COVID-19, we developed a mechanistic, within-host mathematical
41 model and virtual patient cohort. Our results indicate that virtual patients with low production rates of
42 infected cell derived IFN subsequently experienced highly inflammatory disease phenotypes, compared
43 to those with early and robust IFN responses. In these *in silico* patients, the maximum concentration of
44 IL-6 was also a major predictor of CD8⁺ T cell depletion. Our analyses predicted that individuals with
45 severe COVID-19 also have accelerated monocyte-to-macrophage differentiation that was mediated by
46 increased IL-6 and reduced type I IFN signalling. Together, these findings identify biomarkers driving
47 the development of severe COVID-19 and support early interventions aimed at reducing inflammation.

48 **Author summary**

49 Understanding of how the immune system responds to SARS-CoV-2 infections is critical for
50 improving diagnostic and treatment approaches. Identifying which immune mechanisms lead to
51 divergent outcomes can be clinically difficult, and experimental models and longitudinal data are only
52 beginning to emerge. In response, we developed a mechanistic, mathematical and computational model
53 of the immunopathology of COVID-19 calibrated to and validated against a broad set of experimental
54 and clinical immunological data. To study the drivers of severe COVID-19, we used our model to
55 expand a cohort of virtual patients, each with realistic disease dynamics. Our results identify key
56 processes that regulate the immune response to SARS-CoV-2 infection in virtual patients and suggest
57 viable therapeutic targets, underlining the importance of a rational approach to studying novel
58 pathogens using intra-host models.

59 **Introduction**

60 Clinical manifestations of SARS-CoV-2 infection are heterogeneous, with a significant
61 proportion of people experiencing asymptomatic or mild infections that do not require hospitalization.
62 In severe cases, patients develop coronavirus disease (COVID-19) that may progress to acute
63 respiratory distress syndrome (ARDS), which is frequently accompanied by a myriad of inflammatory
64 indicators [1]. Mounting evidence points to a hyper-reactive and dysregulated inflammatory response
65 characterized by overexpression of pro-inflammatory cytokines (cytokine storm) and severe
66 immunopathology as specific presentations in severe COVID-19 [2–6]. An over-exuberant innate
67 immune response with larger numbers of infiltrating neutrophils [7,8] arrests the adaptive immune
68 response through the excessive release of reactive oxygen species that leads to extensive tissue damage
69 and depletion of epithelial cells [9]. In addition, lymphopenia, in particular, is one of the most
70 prominent markers of COVID-19 and has been observed in over 80% of patients [6, 10–12]. However,
71 the immune mechanisms that lead to disparate outcomes during SARS-CoV-2 infection remain to be
72 delineated.

73 Cytokines are critically important for controlling virus infections [13, 14] and are central to the
74 pathophysiology of COVID-19, sometimes playing a detrimental role in the context of a cytokine storm

75 [10]. For example, interleukin-6 (IL-6) can stimulate CD8⁺ T cell expansion under inflammatory
76 conditions [15]; however, in hospitalized SARS-CoV-2 patients with lymphopenia, IL-6 has been
77 shown to be elevated [16] without an increase in CD8⁺ T cell counts [17]. Type I interferons (such as
78 IFNs- α , β [18]) also play a major role in limiting viral replication by inducing a refractory state in
79 susceptible and infected cells [19–21]. Due to this, it has been suggested that a delay in mounting an
80 effective IFN response may be responsible for COVID-19 severity [22] as it is for other highly
81 pathogenic coronavirus (i.e. SARS-CoV and MERS) infections [13]. Overall, patients with severe
82 COVID-19 present with lymphopenia [14, 23], and are likely to have increased inflammatory cytokines
83 such as IL-6, granulocyte-macrophage colony-stimulating factor (GM-CSF), and granulocyte colony-
84 stimulating factor (G-CSF) [7, 17, 24].

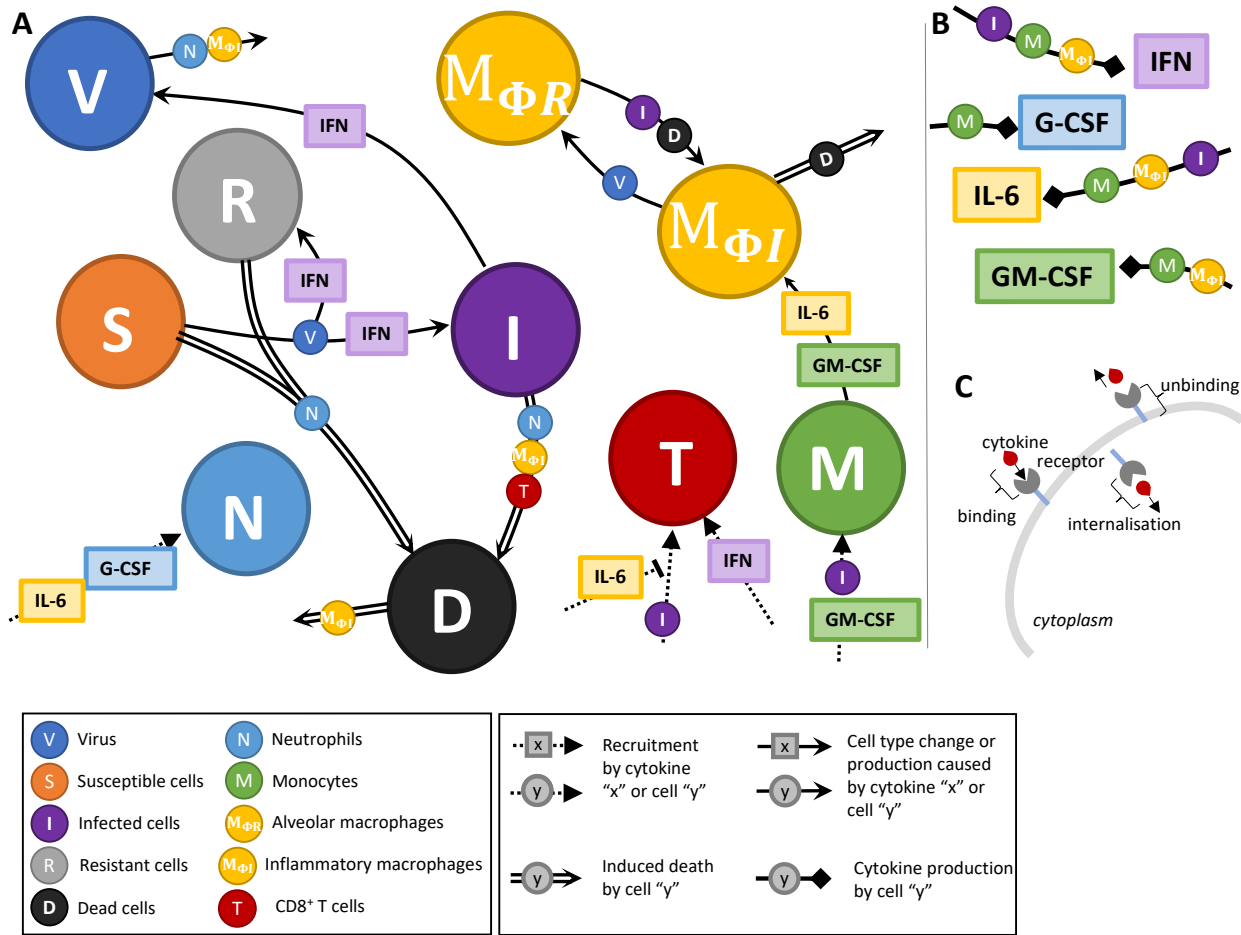
85 Because identifying which immune mechanisms lead to divergent outcomes can be difficult
86 clinically, and experimental models and longitudinal data are only beginning to emerge, theoretical
87 explorations are ideal [25]. Quantitative approaches combining mechanistic disease modelling and
88 computational strategies are being increasingly leveraged to investigate inter- and intra-patient
89 variability by, for example, developing virtual clinical trials [26–28]. More recently, viral dynamics
90 models [29, 30] have been applied to understand SARS-CoV-2 within-host dynamics and their
91 implications for therapy [31–36]. However, there are few comprehensive models that integrate detailed
92 immune mechanisms and allow interrogation of the dynamics controlling divergent outcomes, and
93 none have attempted to quantify the high degree of variability in patient responses to SARS-CoV-2
94 through modelling.

95 In this study, we developed a mechanistic mathematical model to describe the within host
96 immune response to SARS-CoV-2. We explicitly modelled the interactions between epithelial cells,
97 innate and adaptive immune cells and cytokines. The model was fit to various *in vitro*, *in vivo*, and
98 clinical data, analyzed to predict how early infection kinetics facilitate downstream disease dynamics,
99 and used to create a virtual patient cohort with realistic disease courses. Our results suggest that mild
100 and severe disease are distinguished by the rates of monocyte differentiation into macrophages and of
101 IFN production by infected cells. In our virtual cohort, we found that severe COVID-19 responses were
102 tightly correlated with a delay in the peak IFN concentration and that a large increase in IL-6 was the
103 dominant predictor of CD8⁺ T cell depletion in our virtual cohort. Importantly, these results provide
104 insight into differential presentations of COVID-19 by identifying key regulators of severe disease
105 manifestation particularly related to monocyte differentiation and IL-6 concentrations.

106 **Results**

107 **Modelling the immune response to SARS-CoV-2 and the impact of delayed IFN on infection**
108 **dynamics**

109 To study the dynamics of SARS-CoV-2 infection and the development of COVID-19, we
110 constructed a computational biology model of host-pathogen interactions (**Eqs. S1-S22**, with variables
111 and parameters summarized in **Table S1** and schematic in **Figure 1**). The model includes susceptible
112 lung epithelial cells (S) that encounter virus (V) and become infected (I) before turning into damaged
113 or dead cells (D) due to viral infection or immune involvement. The immune response is orchestrated
114 by a myriad of cytokines that act to stimulate the immune cell subsets present in the tissues and recruit
115 cells from the bone marrow and circulation (**Figure 1A**). Upon infection, cells begin secreting type I
116 IFNs (F) that cause lung epithelial cells to become resistant to infection (R) and decrease the
117 production of newly infected cells [37]. Through stimulation by infected and dead cells, alveolar (lung
118 tissue-resident) macrophages ($M_{\phi R}$) become inflammatory macrophages, which also arise through
119 macrophage (M) differentiation by stimulation by GM-CSF (G) or IL-6 (L) [38]. Neutrophils (N) are
120 recruited to the infection site by G-CSF and release reactive oxygen species (ROS) causing bystander
121 damage to infected and susceptible cells [39, 40]. CD8⁺ T cells (T) are subsequently recruited to the
122 infection site following a delay to account for antigen presentation, with expansion modulated by type I
123 IFN and IL-6 concentrations. See **Materials and Methods** for a complete description.



124

125 **Figure 1. Immune response to SARS-CoV-2 infection model schematic.** The model in Eqs. S1-S22 reduced
 126 to **A**) cell dynamics **B**) cytokine production dynamics and **C**) cytokine binding kinetics. Unique lines represent
 127 induced cell death (double line), recruitment (dashed line), cell type change or production (solid line), and
 128 cytokine production (square arrow). Cell and/or cytokines along joining lines denote a causal interaction. **A**)
 129 Virus (*V*) infects susceptible lung epithelial cells and creates either infected (*I*) or resistant (*R*) cells depending
 130 on the concentration of type I IFN. Infected cells then either die and produce new virus or are removed via
 131 inflammatory macrophages ($M_{\phi I}$) or CD8⁺ T cells (*T*) that induce apoptosis to create dead cells (*D*). Neutrophils
 132 (*N*) cause bystander damage (death) in all epithelial cells and are recruited by individually G-CSF and IL-6
 133 concentrations. CD8⁺ T cells are recruited by infected cells and their population expands from IFN signalling. T
 134 cell recruitment is inhibited by IL-6 concentrations. Monocytes (*M*) are recruited by infected cells and GM-CSF
 135 and differentiate into inflammatory macrophages based on the individual concentrations of GM-CSF and IL-6.
 136 Tissue-resident macrophages ($M_{\phi R}$) also become inflammatory macrophages through interaction with dead and
 137 infected cells. Dead cells are cleared up by inflammatory macrophages and also cause their death. **B**) Type I IFN
 138 is produced by infected cells, inflammatory macrophages and monocytes. G-CSF is produced solely by
 139 monocytes and GM-CSF is produced by monocytes and macrophages. IL-6 is produced by monocytes,
 140 inflammatory macrophages and infected cells. **C**) Cytokine receptor binding, internalization and unbinding
 141 kinetics considered for each cell-cytokine interaction.

142

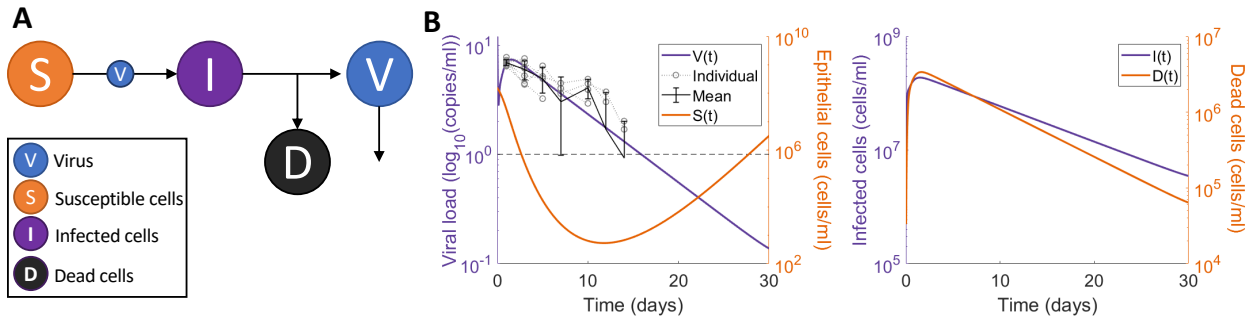
143

144

145

Because the model has several parameters that are undetermined biologically and insufficient data exists to confidently estimate their values, we used a stepwise approach to parameter estimation (see **Materials and Methods** and **Figures S1-S5**). We first confirmed that we could recapitulate early infection viral kinetics with a reduced version of the full model ('viral model'). For this, we excluded

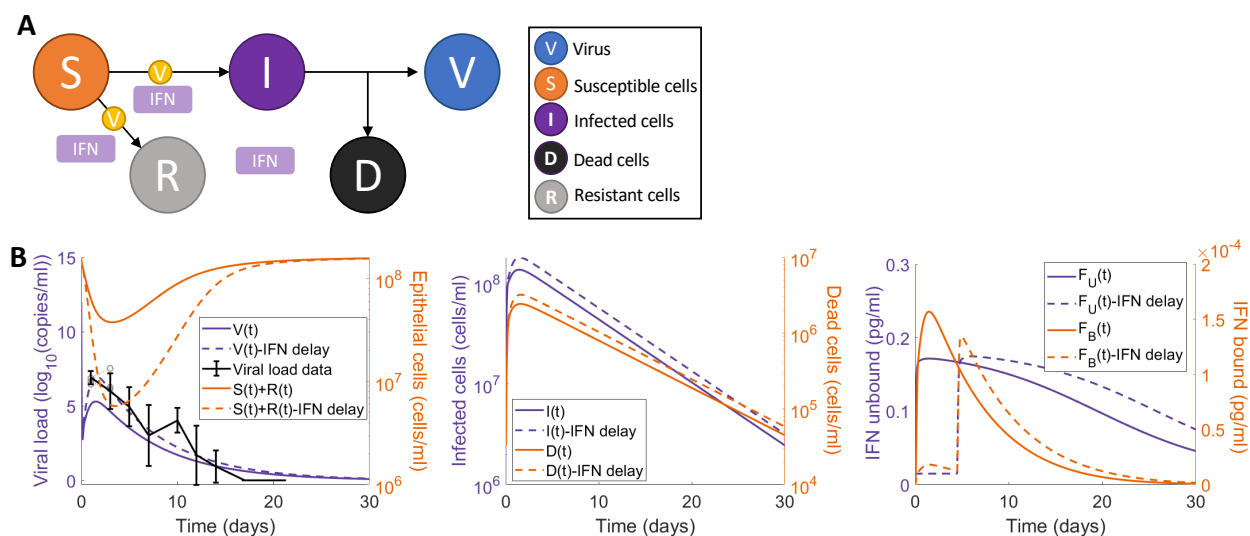
146 immunological variables (i.e. only including **Eqs. 6-9**) and estimated parameters relating to viral
147 kinetics by fitting to viral load data from macaques (see **Materials and Methods**). The resulting model
148 dynamics were in good agreement to these early infection data (**Figure 2**) and demonstrate a rebound
149 in epithelial lung tissue as the viral load and infected cells decrease.



150

151 **Figure 2. Viral dynamics model fit to macaque viral data from Munster et al. [41]** A reduced version of the
152 full model (all cytokine and immune cells set to 0, **Eqs. 6-9**) was fit to data from macaques [41] to estimate
153 preliminary viral kinetic parameters. **A)** Virus (V) infects susceptible cells (S) making infected epithelial cells (I)
154 which then die to produce dead cells (D) and new virus. **B)** Comparison of predicted viral dynamics compared to
155 observations from 6 animals, with susceptible cell kinetics (left) with predictions of infected and dead cells over
156 time (right). We estimated β , p , d_I , V_0 and d_V from the reduced model in **A)** fit to data from Munster et al. [41]
157 measuring the viral load in macaques after challenge with SARS-CoV-2 (**Table S1**).

158 We then isolated the IFN dynamics to assess clinical and experimental findings suggesting that
159 delaying IFN results in more severe presentations in highly pathogenic coronavirus infections including
160 SARS-CoV-2 [13, 14, 22]. Using the parameters obtained from the ‘viral model’ (**Eqs. 6-9; Table S1**),
161 we then simulated the impact of IFN with the ‘IFN model’ (**Eqs. 10-16 and Figure 3A**). We examined
162 the predicted dynamics in response to delayed IFN by simulating with and without a fixed delay for
163 IFN production from infected cells. Our results suggest that delaying type I IFN production by 5 days
164 yields a 10-fold increase in tissue damage with only 20% of the lung tissue remaining on day 2 (**Figure**
165 **3B**), caused by the increase in infected cells and subsequent lack of resistant cells. IFN dynamics were
166 matched to systemic IFN- α concentrations from clinical cohorts by visual predictive check to confirm
167 that predictions fell within the observed ranges [42] (**Figure S6A**).



168

169

170

171

172

173

174

Figure 3. Delayed type I IFN response impacts heavily on tissue survival in reduced model. **A)** Submodel (Eqs. 10-16) with all non-IFN cytokines and immune cell interactions set to zero and only considering interactions between virus (V) and susceptible (S), infected (I), resistant (R), and dead (D) epithelial cells. **B)** Predictions from the simplified model without delayed IFN production (solid lines) versus with a constant delay ($\tau_F = 5$ days) (dotted lines). Solid black (left panel): viral loads from SARS-CoV-2 infection in macaques by Munster et al. [41] is overlaid with predicted viral dynamics.

175

Immunologic determinants of mild and severe disease

176

177

178

179

180

181

182

183

184

185

186

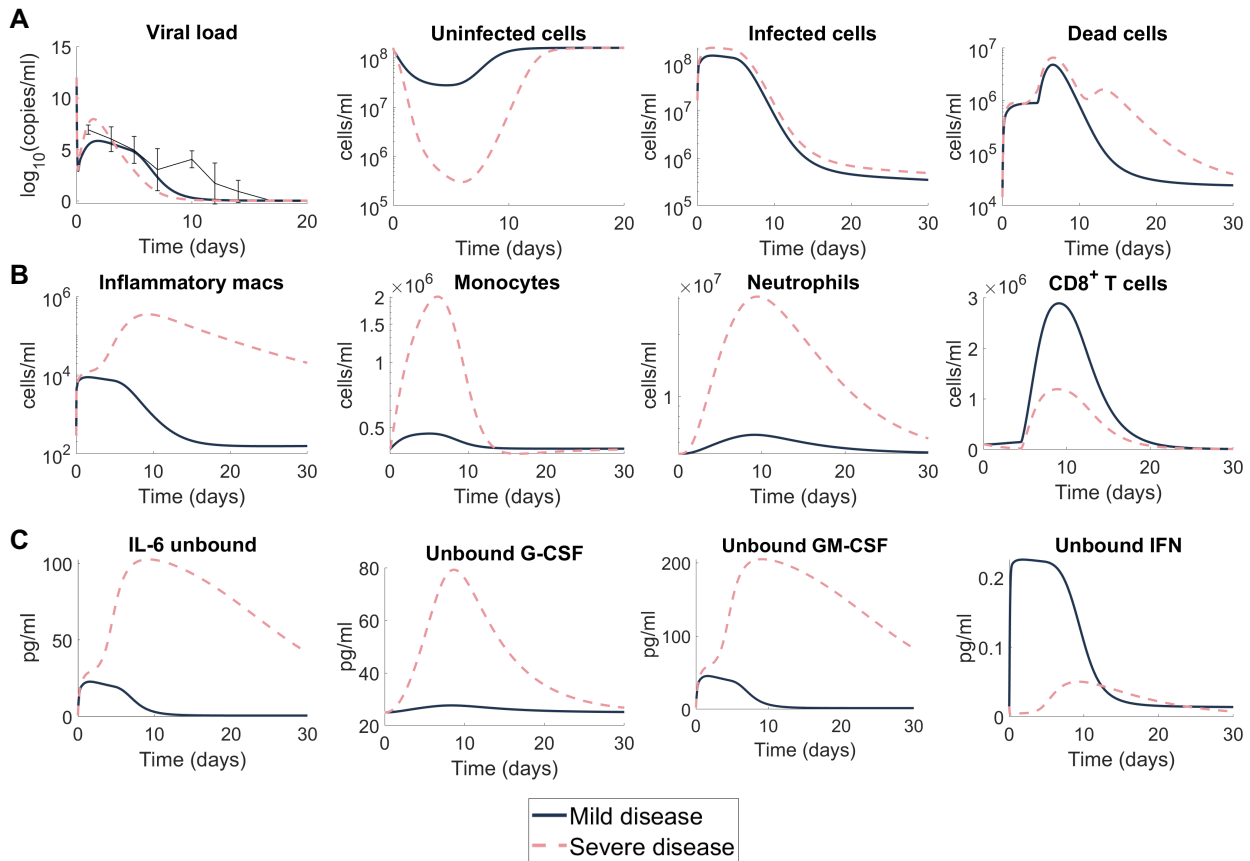
187

188

189

190

Next, to establish the mechanisms that differentiate mild versus severe disease, we simulated the full model (Eqs. S1-S22) using two different parameter sets. Mild disease dynamics were recreated using the estimated parameter values (Table S1) with the virus decay rate (d_V) and the infected cell death rate (d_I) recalculated to ensure that the maximum death rate of the virus and infected cells did not exceed the value obtained from the reduced viral dynamics model fit (Figure 2). Simulating mild disease, we predicted that all cell populations and cytokines rapidly return to homeostasis, with the immune response effectively clearing virus within 10 days (Figure 4 and Figure S7). Because severe SARS-Cov-2 infection results in lower levels of IFN [42] and increased monocytes [43], we recapitulated severe disease by modulating model parameters relating to these processes, i.e., the rates of IFN production from infected cells and macrophages were decreased, and the rate of monocyte recruitment from the bone marrow by infected cells was increased. With these changes, the model predicted a dramatic shift in disease response that was characterized by a cytokine storm (elevated IL-6, GM-CSF and G-CSF), high ratios of innate to adaptive immune cells, and a marked reduction in healthy viable lung tissue (Figure 4A), whereas changes in viral load remained relatively consistent with mild disease.



191

192 **Figure 4. Predicting mild and severe COVID-19 dynamics.** Mild disease (solid lines) dynamics obtained by
 193 using baseline parameter estimates (**Tables S1**) while severe disease dynamics (dashed lines) were obtained by
 194 decreasing the production rate of type I IFN ($p_{F,I}$) and increasing the production of monocytes ($p_{M,I}$) and their
 195 differentiation to macrophages ($\eta_{F,M\phi}$). **A**) Viral load and lung cells concentrations (susceptible, resistant,
 196 uninfected, and dead cells). Solid black line with error bars indicates macaque data [41] (see **Figure 2**). **B**) Immune
 197 cell concentrations (inflammatory macrophages, monocytes, neutrophils, and CD8⁺ T cells. **C**) Unbound
 198 cytokine concentrations (free IL-6, GM-CSF, G-CSF, and type I IFN). Time evolution of all model variables is
 199 shown in **Figure S7** (including bound cytokine and alveolar macrophages).

200

201 In addition, there was a significant increase in the number of inflammatory macrophages
 (Figure 4B), IL-6, GM-CSF and, importantly, a delayed and reduced IFN peak (Figure 4C). In
 202 comparison to the mild disease, inflammatory macrophages and neutrophils (Figure 4B) remained
 203 elevated for at least 30 days after initial infection. Comparing mild and severe disease highlighted
 204 significant differences in the area under the curve (AUC) of macrophages (6×10^4 cells/ml versus
 205 3×10^{11} cells/ml) and neutrophils (2×10^8 cells/ml versus 3×10^{13} cells/ml) over 30 days.

206

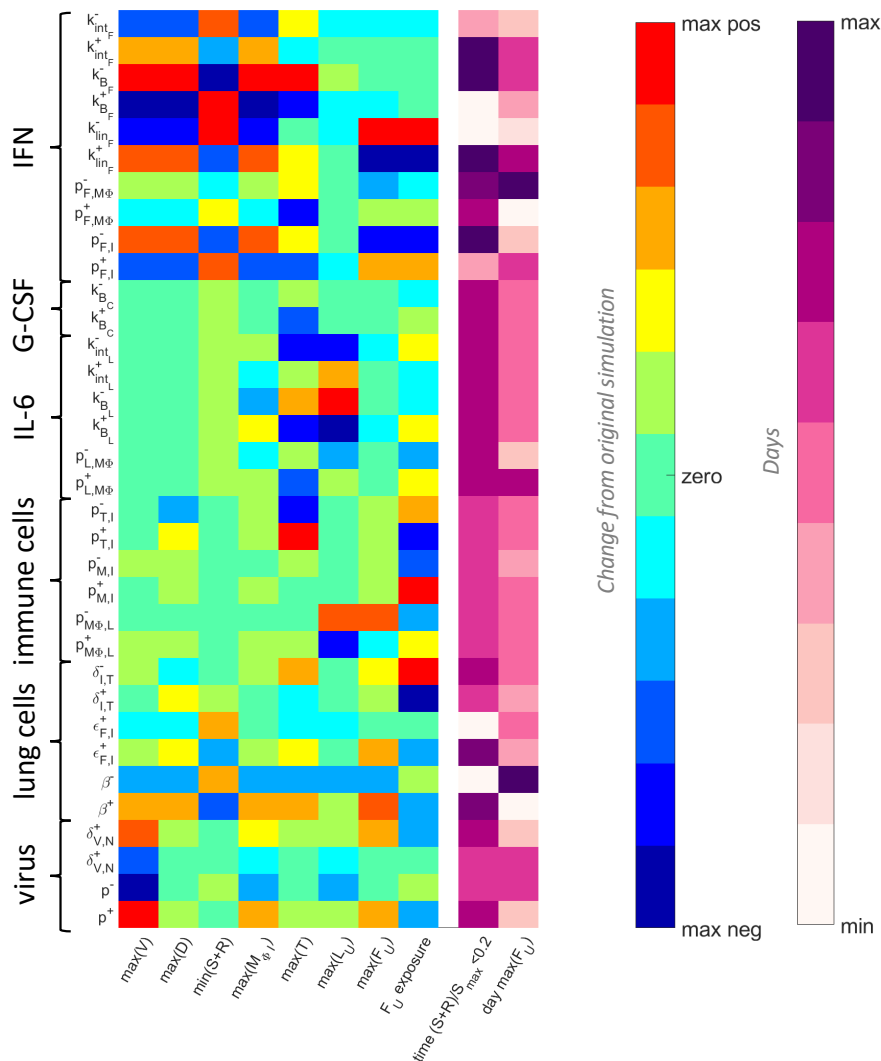
207 Interestingly, inflammation remained high in the severe disease scenario despite the virus being
 208 cleared slightly faster (~ 1 day) than in the case of mild disease (Figure 4A). Further, the peak of
 209 inflammatory macrophages increased from $\sim 10^4$ cells/ml to $\sim 10^6$ cells/ml in severe scenarios
 210 compared to mild scenarios (Figure 4B). The model also accurately predicted that CD8⁺ T cell
 dynamics were lower in severe cases, which is indicative of lymphopenia and similar to clinical

211 observations from patients with severe COVID-19 [14, 23]. Despite varying only three parameters to
212 generate disparate dynamics, the immune cell and cytokine dynamics were qualitatively in line with
213 clinical observations for IFN- α [42], IL-6 [42, 44], and G-CSF [24] (**Figure S6B-F**).

214 **Macrophages, CD8⁺ T cells, IFN and IL-6 regulates response to SARS-CoV-2 infection**

215 To further understand how the host immune system regulates the response to SARS-CoV-2
216 infection, we conducted a local sensitivity analysis by varying each parameter individually by $\pm 20\%$
217 and comparing a set of metrics (see **Materials and Methods**) chosen to provide a comprehensive
218 understanding of each parameter's impact on the host-pathogen dynamics. This analysis identified 17
219 sensitive parameters (**Figure 5**) relating to virus productivity ($p, \delta_{V,N}, \beta, \epsilon_{F,I}$), CD8⁺ T cell induced
220 epithelial cell apoptosis ($\delta_{I,T}$), macrophages, monocyte and CD8⁺ T cell production ($p_{M\Phi,L}, p_{M,I}, p_{T,I}$),
221 IL-6 ($p_{L,M\Phi}, k_{BL}, k_{intL}$), G-CSF (k_{BC}), and IFN ($p_{F,I}, p_{F,M\Phi}, k_{linF}, k_{BF}, k_{intF}$).

222 The rate of viral infectivity (β) had a particularly significant impact on all metrics where
223 increases resulted in higher viral loads and longer periods of tissue damage $> 80\%$. The duration of
224 extensive tissue damage ($>80\%$ damaged) also increased with IFN potency ($\epsilon_{F,I}$). Decreasing the rate
225 of IL-6-induced monocyte differentiation into inflammatory macrophages ($p_{M\Phi,L}$) increased the peak of
226 both IL-6 and IFN. Notably, changes to parameters that increased the bound IFN concentration, i.e.
227 increasing the binding and production rates (k_{BF} and $p_{F,I}$) and decreasing the internalization and
228 clearance rates (k_{linF} and k_{intF}) induced significant changes in most metrics (**Figure 5**). See **Figure S8**
229 for complete sensitivity analysis results.



230 **Figure 5. Parameters driving COVID-19 severity.** A local sensitivity analysis was performed by varying each
 231 parameter $\pm 20\%$ from its originally estimated value and simulating the model. Predictions were then compared
 232 to baseline considering: Maximum viral load ($\max(V)$), maximum concentration of dead cells ($\max(D)$),
 233 minimum uninfected live cells ($\min(S+R)$), maximum concentration of inflammatory macrophages ($\max(M_{\phi I})$),
 234 maximum number of $CD8^+$ T cells ($\max(T)$), maximum concentration of IL-6 ($\max(L_U)$), maximum
 235 concentration of type I IFN ($\max(F_U)$), the total exposure to type I IFN (F_U exposure), the number of days
 236 damaged tissue was $>80\%$ ($\text{time}(S+R)/S_{max}$), and the day type I IFN reached its maximum ($\text{day max}(F_U)$).
 237 The heatmaps show the magnitude change of each metric, where blue signifies the minimum value observed and
 238 red signifies the maximum value observed, or by the number of days, where light to dark pink signifying
 239 increasing number of days from zero. The most sensitive parameters are shown here (for complete parameter
 240 sensitivity results, see **Figure S8**).

241 Virtual patient cohort identifies heterogeneity in immune dynamics and severity

242 To better understand the clinical variability in SARS-CoV-2 infection severity [1], we next
 243 generated a cohort of 200 virtual patients (see **Materials and Methods** and **Figure 7**). To create each
 244 *in silico* patient, seven patient-specific parameters were sampled from normal distributions with means
 245 corresponding to their respective fixed values and standard deviations inferred from clinical
 246 observations (**Table 1**). In doing this, we assumed intrinsic interindividual heterogeneity in monocyte

247 to macrophage differentiation, production of IL-6 by macrophages, recruitment of macrophages by the
 248 presence of infected cells, and production of IFN by infected cells, macrophages and monocytes,
 249 respectively.

250 Parameters were chosen based on their impact on maximum IL-6 and IFN levels as well as
 251 tissue damage observed in the sensitivity analysis ($p_{M\Phi,I,L}$, $p_{L,M\Phi}$, $p_{F,I}$, $p_{M,I}$, and $\epsilon_{F,I}$; **Figure 5**). In
 252 addition, we designated patient-specific parameters accounting for alternate pathways through which
 253 IFN is affected by innate immune cells ($\eta_{F,M\Phi}$ and $p_{F,M}$). For the production of IL-6 by macrophages
 254 and monocyte to macrophage differentiation via IL-6 stimulation, standard deviations were inferred
 255 from IL-6 levels in non-mechanically ventilated patients (mild) and from mechanically ventilated
 256 patients (severe) [44] (**Figure S7D**). Standard deviations for the production of IFN by infected cells
 257 were determined from the 95% confidence interval for IFN- α from Trouillet-Assant et al. [42] (**Figure**
 258 **S7A-B**), and, lastly, the standard deviation for the production of IFN by macrophages was obtained
 259 from the 95% confidence interval in Sheahan et al. [45]. The variation in virtual patient responses was
 260 then constrained by experimental and clinical viral loads, IFN, neutrophil, IL-6, and G-CSF (**Figure 7**).
 261 The resulting cohort dynamics were within ranges for IFN and IL-6 measurements in asymptomatic to
 262 severe COVID-19 patients in the literature [11, 17] (**Figure S9**).

Para m	Units	Description	Mean	Ref	Std Dev	Ref	Range
$p_{M\Phi,I,L}$	1/day	Monocyte to macrophage differentiation by IL-6	1.7	[46]	2.2	[7]	[0, 9.9]
$p_{L,M\Phi}$	pg/ml/day	IL-6 production by activated macrophages	1872	[47]	2.2	[7]	[1863, 1880]
$p_{F,I}$	pg/ml/day	IFN production by infected cells	2.82	[48]	1.9	[44]	[0, 12.2]
$p_{M,I}$	1/day	Monocyte recruitment rate by infected cells	0.22	[49]	0.08	[50]	[0, 0.63]
$\eta_{F,M\Phi}$	10^9 cells/ml	IFN by infected cells	0.001 2	[48]	10^{-5}	[51]	[0, 10^{-4}]
$\epsilon_{F,I}$	pg/ml	IFN production of CD8 ⁺ T cells	0.004	[52]	10^{-5}	[45]	[0, 10^{-4}]
$p_{F,M}$	pg/ml/day	IFN production by monocytes	3.56	[53, 54]	0.013	[53]	[3.4, 3.6]

263 **Table 1 Virtual patient-specific parameter values.** Seven parameters in the model were deemed patient-
 264 specific and were drawn from a normal distribution with mean the parameter value obtained either through
 265 fitting or from the literature (**Table S1**). The standard deviation (Std Dev) for each normal distribution was
 266 informed by values in the literature (see **Materials and Methods** and Supplementary Information Sections
 267 S6.1). Initial parameter sampling and new parameters generated through the simulated annealing optimization,
 268 were bounded within the interval range noted. All other parameters in the model were fixed to their original
 269 value (**Table S1**).

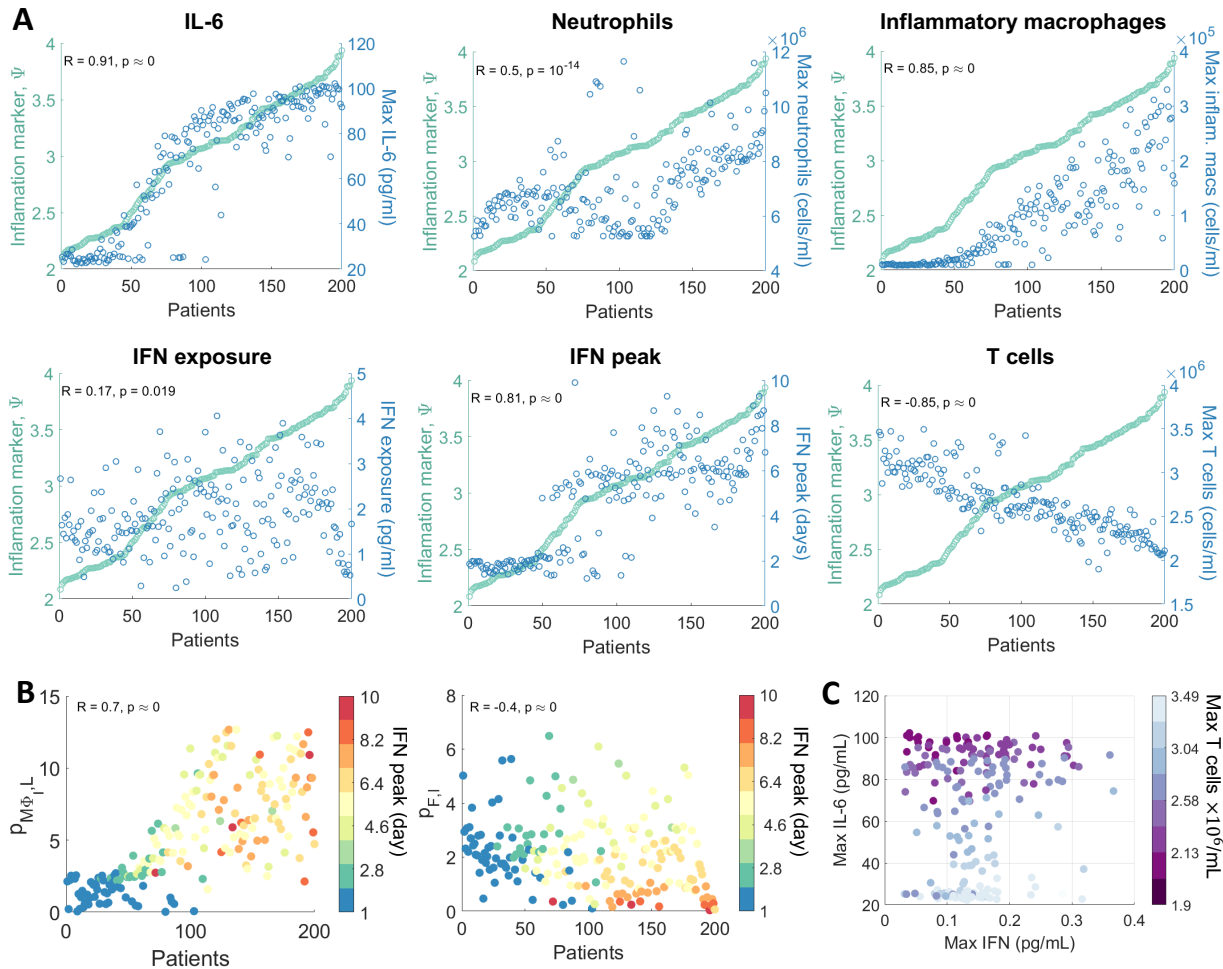
270 To quantify disease severity, we introduced an inflammation variable, Ψ , that measured
271 maximum IL-6, neutrophils and tissue damage (**Eq. 18**) and then compared it to individual
272 characteristics of each virtual patient's disease. We evaluated each virtual patient's maximum IL-6,
273 CD8⁺ T cells, and neutrophils; minimum percentage of healthy lung tissue; the time to peak IFN; and
274 total IFN exposure (area under the curve or AUC) within 21 days of infection. Ordering patients by
275 their value of Ψ and plotting the corresponding values for different characteristics evaluated showed a
276 clear separation between those with mild disease and those with severe disease (**Figure 6A**).

277 Patients with higher inflammation had higher IL-6, neutrophil, and inflammatory macrophage
278 concentrations (**Figure 6A**). While the IFN exposure was not significantly stratified by Ψ , the peak of
279 IFN and CD8⁺ T cell levels were strongly negatively correlated with the inflammation marker ($R =$
280 -0.85 , $p < 1 \times 10^{-9}$, see **Materials and Methods**). IL-6 was most noticeably correlated with Ψ ($R =$
281 0.91 , $p < 1 \times 10^{-9}$), with a distinct upper bound in the concentration (~ 100 pg/ml) achieved in 50% of
282 the virtual cohort. There appeared to be a transition phase in inflammation driven by neutrophil levels
283 where patients with moderate inflammation ($3 < \Psi < 3.5$) had low counts (less than 7×10^6 cells/ml)
284 compared to patients with more severe inflammation ($\Psi \geq 3.5$) who had higher levels ($p =$
285 1.46×10^{-6}). Despite this, patients with moderate inflammation exhibited increased disease markers
286 including delayed IFN peaks and lower CD8⁺ T cells, compared to patients with mild inflammation
287 ($\Psi \leq 3$).

288 A distinct jump in the timing of the IFN peak in the virtual cohort ($p < 1 \times 10^{-5}$) was
289 correlated with inflammation, as patients with low inflammation ($\Psi \leq 3$) had peaks at day 2 compared
290 to day 6 in patients with higher inflammation ($\Psi > 3$). Grouping virtual individuals by their time to IFN
291 peak suggests that those with IFN peaks after day 3 of infection also had fewer macrophages ($p <$
292 1×10^{-5}) and larger numbers of CD8⁺ T cells ($p < 1 \times 10^{-5}$). Overall, delays in IFN peak did not
293 cause significant changes to viral load but were sufficient to cause major tissue damage (100x
294 reduction in viable tissue remaining) and over-heightened immune responses (4x increase in maximum
295 IL-6 and GM-CSF concentrations).

296 We found a positive correlation ($R = 0.67$, $p = 1.58 \times 10^{-8}$) between the time to peak IFN
297 concentration for each patient against their IFN production rate from infected cells (**Figure 6B**).
298 Interestingly, the time to peak IFN for each patient was also strongly related to their rate of IL-6-
299 stimulated monocyte differentiation into macrophages. Low IFN production rates were predominately
300 responsible for significantly delayed IFN peaks over 6 days after infection, whereas IFN peaks within 3
301 days of infection were largely caused by lower rates of monocyte to macrophage differentiation.

302 Further, examining the relationship between each virtual patient’s maximum IL-6, IFN, and CD8⁺ T
 303 cell concentrations (**Figure 6C**) identified a weaker correlation between the maximum concentration of
 304 CD8⁺ T cells and IFN ($R = 0.24, p = 0.0008$) as opposed to with IL-6 ($R = -0.86, p < 1 \times 10^{-9}$).



305
 306 **Figure 6. Virtual Cohort of SARS-CoV-2 infected patients.** 200 virtual patients were generated by sampling
 307 parameters related to macrophage, IL-6, and IFN production ($p_{M\Phi,I,L}, p_{L,M\Phi}, p_{F,I}, p_{M,I}, \eta_{F,M\Phi}, \epsilon_{F,I},$ and $p_{F,M}$) from
 308 normal distributions with mean equal to their original values and standard deviation inferred from clinical
 309 observations (**Figure 7**). Each virtual patient had a distinct parameter set that was optimized to that patient’s
 310 dynamics in response to SARS-CoV-2 infection corresponded to physiological intervals reported in the literature
 311 (see **Materials and Methods**). **A**) Infection and immune response metrics (blue) in individual patients were
 312 compared to inflammatory variable Ψ (green). Each point represents an individual patient, ordered according to
 313 Ψ . The correlation coefficient (R) and p -value are indicated for each, with $\alpha < 0.05$ denoting significant
 314 correlations. **B**) Parameters most correlated to the IFN peak time were the rates of macrophage production via
 315 IL-6 ($p_{M\Phi,I,L}$) and the IFN production by infected cells ($p_{F,I}$). Individual patient values for these parameters are
 316 plotted as circles coloured by the patient’s corresponding day of IFN peak (see color bar). Patients are ordered
 317 by their inflammation marker Ψ . **C**) Correlations between maximal IFN, IL-6, and T cell concentrations for each
 318 patient (circles). Circle colour corresponds to the maximal T cell concentration of each patient.

319 Discussion

320 Serial immunological measurements from COVID-19 patients are only beginning to be
 321 collected, and the ability to assess initial infection kinetics and the drivers of the ensuing disease

322 remains limited. The data-driven mechanistic mathematical model and virtual patient cohort developed
323 here identified important immunological drivers of COVID-19. In particular, to recreate severe
324 dynamics, it was sufficient to vary only two processes in the model: the rates of type I IFN production
325 from infected cells and macrophages, and the rate of monocyte recruitment by infected cells. This
326 suggests that the distinction between severe and mild disease may be driven by a limited set of causal
327 regulators. The effect on IFN production may be further exacerbated by autoimmunity against type I
328 IFNs, which has been shown to correlate to life-threatening COVID-19 pneumonia in 2.6% of women
329 and 12.5% of men [18].

330 Our results show that delaying type I IFN production is sufficient to cause major tissue damage
331 and heightened immune responses yet have little impact on peak viral loads. In the severe disease
332 simulation, viral load was cleared marginally faster (~1 day) in comparison to the mild disease
333 simulation. This finding is supported by recent clinical evidence showing that an increased rate of viral
334 decline rather than peak viral load may be more predictive of disease severity [6]. This therefore
335 suggests that viral load may not be a necessary attribute to obtain severe tissue damage. Instead, our
336 model predicts that increases in tissue damage occur through heightened innate immune responses.
337 Evaluating SARS-CoV-2 infection in a cohort of 200 virtual patients revealed several immunological
338 responses responsible for differential disease presentation. Notably, a distinct, emergent switch in the
339 type I IFN response corresponded with late IFN peaks and more severe disease (i.e., higher
340 inflammation Ψ). This supports previous findings that connect a delay in type I IFN with more severe
341 presentations of highly pathogenic coronaviruses infections including SARS-CoV, MERS-CoV, and
342 SARS-CoV-2 [13, 14, 22]. Virtual patients with rates of monocyte differentiation close to the rate at
343 homeostasis tended to achieve peak IFN concentrations approximately 2 days after infection compared
344 to those with higher inflammation and later IFN responses, who had at least a 3-fold increase in this
345 rate. This switch in timing was caused by increased rates of monocyte-to-macrophage differentiation
346 and decreased production of IFN by infected cells, with the initial delay of IFN caused by increased
347 monocyte differentiation and the more extreme IFN delays caused by IFN production from infected
348 cells, indicating that the timing of the IFN peak in a patient may allow for improved stratification into
349 treatment arms designed to target one or both of these responses. The finding that IFN binding was
350 predictive of the duration of lung tissue damage, suggests that virus-intrinsic properties and their ability
351 to inhibit receptor mediated binding and endocytosis could delay IFN production and cause
352 downstream increases in IL-6 and GM-CSF resulting in severe disease. Our results further highlight
353 that lymphopenia is tightly correlated with maximum IL-6 concentration and less dependent on the
354 timing of IFN.

355 The ability of our model to recapitulate severe disease by, in part, regulating monocyte
356 differentiation raises the possibility that patients with low monocyte levels [7] may benefit from
357 treatments that better regulate monocyte differentiation. This is in line with recent studies identifying
358 distinct transcriptional factors as regulators of differentiated monocyte fates in inflammatory conditions
359 [55, 56]. It also raises the possibility that modulation by exogenous cytokines, including macrophage
360 colony-stimulating factor in combination with IL-4 and tumour necrosis factor-alpha (TNF- α), may be
361 able to direct monocyte differentiation in favour of monocyte-derived dendritic cells and reduce this
362 response [55]. Recently, the neutralization of both TNF- α and IFN- γ has been found to benefit patients
363 with COVID-19 or other cytokine storm-drive syndromes by limiting inflammation and tissue damage
364 [57]. Given that TNF- α also has a secondary benefit on monocyte differentiation, our results support
365 the viability of this avenue of treatment. Caution should be noted, however, given that previous
366 attempts to regulate host responses by IL-6 blockade have proven unsuccessful [58].

367 Together, our findings support the idea that early interventions aimed at reducing inflammation
368 are more likely to be beneficial for patients at risk of progressing to severe COVID-19 than attempts to
369 inhibit cytokine storm later in the disease course, given that early IFN responses were found to provoke
370 better controlled immune responses and outcomes in our virtual cohort. It will be essential to
371 characterize both the timing and mechanisms of proposed therapeutic interventions to develop effective
372 treatments to mitigate severe disease.

373 **Materials and Methods**

374 **Mathematical model of the immune response to SARS-CoV-2**

375 Our model was developed to examine SARS-CoV-2 infection dynamics and identify
376 immunological drivers of disease severity (**Eqs. S1-S22**). Throughout, cytokine and immune cell
377 interactions and effects were described by Hill functions as

$$\frac{B^h}{B^h + \gamma^h} I$$

378 where B is the interacting compound, γ its half-effect value, and h the Hill coefficient [59, 60]. Further,
379 for a given cytokine X and cell population Y , the production (recruitment/differentiation) rate of X by Y
380 was denoted by $p_{X,Y}$ and the rate of production of Y by X by $p_{Y,X}$. The half-effect concentration (i.e. γ
381 in **Eq. 1**) of cytokine X on cell population Y was represented by $\epsilon_{X,Y}$ and the half-effect concentration
382 of cell Y affecting cytokine X was given by $\eta_{X,Y}$. The natural death rate of cell Y was denoted by d_Y ,
383 and the rate of induced death of cell Y by cell Z by $\delta_{Y,Z}$. Lastly, the carrying capacity concentration of
384 cell Y was denoted by Y_{max} , and regeneration or proliferation rates by λ_Y .

385 We modelled virus (V) being produced by infected cells at rate p and cleared via exponential
386 clearance at rate d_V , which accounts for all contributions to viral degradation except macrophage- and
387 neutrophil-mediated clearance. Immune-mediated viral clearance via phagocytosis by inflammatory
388 macrophages [61] and neutrophil extracellular traps (NETs—extracellular chromatin fibres produced
389 by neutrophils to control infections) [39, 40] was considered to occur at rates $\delta_{V,M\Phi I}$ and $\delta_{V,N}$,
390 respectively. Susceptible epithelial cells (S) grow logistically with per capita proliferation rate λ_S and
391 carrying capacity S_{max} , and become infected (I) at rate β . The damage inflicted on epithelial cells by
392 neutrophils was modelled using a Hill function (**Eq. 1**) [60], where neutrophils kill/damage epithelial
393 cells at rate δ_N through the release of NETs and other antimicrobials proteins [39, 40]. The constant ρ
394 ($0 < \rho < 1$) was included to modulate bystander damage of uninfected cells (S and R).

395 For the purposes of our investigation, we only considered type I IFN dynamics (primarily IFN-
396 α, β). Type I IFN (F_U and F_B) reduces the infectivity and replication capability of viruses by stimulating
397 cells to become resistant to infection. These resistant cells (R) proliferate at a rate equivalent to
398 susceptible cells (λ_S). The concentration of bound IFN (F_B) modulates the creation of infected and
399 resistant cells [19, 21, 62, 63], where increasing the concentration of IFN causes more cells to become
400 resistant to infection and less to become productively infected (I). The potency of this effect is
401 controlled by the half-effect parameter $\epsilon_{F,I}$. Following the eclipse phase (which lasts τ_I hours),
402 productively infected cells (I) produce virus before undergoing virus-mediated lysis at rate d_I .
403 Although various immune cell subsets contribute to infected cell clearance, we limited our
404 investigation to macrophages and effector CD8⁺ T cells which induce apoptosis at rates $\delta_{I,M\Phi}$ and $\delta_{I,T}$,
405 respectively.

406 The accumulation of dead cells (D) was assumed to occur through infected cell lysis d_I ,
407 neutrophil damage/killing of epithelial cells δ_N , macrophage phagocytosis of infected cells $\delta_{I,M\Phi}$,
408 macrophage exhaustion $\delta_{M\Phi,D}$, and CD8⁺ T cell killing of infected cells $\delta_{I,T}$. These dead cells
409 disintegrate relatively quickly [64] at rate d_D , and are cleared through phagocytosis by macrophages
410 [65] at rate $\delta_{D,M\Phi}$.

411 Resident alveolar macrophages ($M_{\Phi R}$) are replenished at a logistic rate inversely proportion to
412 viral load with maximal rate of $\lambda_{M\Phi}$ and half-effect $\epsilon_{V,M\Phi}$ (i.e. as the virus is cleared, the inflammatory
413 macrophage pool replenishes the alveolar macrophage population in the lung). We modelled the
414 transition of alveolar macrophages to inflammatory macrophages ($M_{\Phi I}$) as dependent on infected and
415 dead cells, with a maximal rate of $a_{I,M\Phi}$. Resident macrophages die naturally at a rate $d_{M\Phi R}$ or due to
416 the clearing of dead cells (exhaustion) [65] at rate $\delta_{M\Phi,D}$.

417 Inflammatory macrophages are produced by three distinct pathways (acting individually or in
 418 concert): 1) stimulated tissue-resident macrophages $a_{I,M\Phi}$, (2) GM-CSF-dependent monocyte
 419 differentiation, with maximal production $p_{M,G}$ and half effect $\epsilon_{G,M}$, and (3) IL-6-dependent monocyte
 420 differentiation, with maximal production rate $p_{M\Phi,IL}$ and half-effect $\epsilon_{L,M\Phi I}$. We assumed that
 421 inflammatory macrophages die naturally at rate $d_{M\Phi I}$ or from clearing dead cells at a rate $\delta_{M\Phi,D}$.

422 We have previously shown that endogenous cytokine concentrations are far from quasi-
 423 equilibrium at homeostasis [66]. Therefore, to describe the pharmacokinetics and pharmacodynamics
 424 of cytokine binding and unbinding, we leveraged the framework established in Craig et al. [66] (**Figure**
 425 **1C**) for IFN (F_B and F_U), IL-6 (L_B and L_U), GM-CSF (G_B and G_U), and G-CSF (C_B and C_U). In its
 426 general form, this pharmacokinetic relationship is expressed as

$$\frac{dY_U}{dt} = Y_{prod} - k_{lin}Y_U - k_B(XA - Y_B)(Y_U)^{POW} + k_UY_B, \quad 2$$

$$\frac{dY_B}{dt} = -k_{int}Y_B + k_B(XA - Y_B)(Y_U)^{POW} - k_UY_B \quad 3$$

427 where Y_U and Y_B are free and bound cytokines, Y_{prod} is the rate of endogenous cytokine production, k_B
 428 and k_U are the respective binding and unbinding rates, k_{int} is the internalization rate of bound cytokine,
 429 and k_{lin} is the elimination rate. Here, POW is a stoichiometric constant, A is a scaling factor and X is
 430 the sum of all cells modulated by the cytokine with

$$XA = \hat{p}Y_{MW}K10^nX. \quad 4$$

431 where \hat{p} is a constant relating the stoichiometry between cytokine molecules and their receptors, K is
 432 the number of receptors specific to each cytokine on a cell's surface and 10^n is a factor correcting for
 433 cellular units (see **Eqs. S19-S22**). The molecular weight was calculated in the standard way by dividing
 434 the cytokine's molar mass (MM) by Avogadro's number ($Y_{MW} = MM/6.02214 \times 10^{23}$).

435 We considered unbound IL-6 (L_U) to be produced from productively infected cells,
 436 inflammatory macrophages, and monocytes, with bound IL-6 (L_B) resulting from binding to receptors
 437 on the surface of neutrophils, CD8⁺ T cells and monocytes. Unbound GM-CSF (G_U) was assumed to be
 438 produced from inflammatory macrophages and monocytes and bind to receptors on monocytes to
 439 create bound GM-CSF (G_B). GM-CSF can be produced by CD8⁺ T cells [67], but this was excluded
 440 because it was insignificant to the full system's dynamics. Unbound G-CSF (C_U) is secreted by
 441 monocytes, with bound G-CSF (C_B) produced via binding to neutrophil receptors. Lastly, because
 442 unbound type I IFNs (F_U) are known to be produced by multiple cell types in response to viral
 443 infection, including lymphocytes, macrophages, endothelial cells and fibroblasts [62], we modelled its

444 unbound production from infected cells, infiltrating/inflammatory macrophages, and monocytes, and its
445 binding to receptors on both CD8⁺ T cells and infected cells (**Figure 1B**).

446 The pharmacokinetics and pharmacodynamics of G-CSF on neutrophils (N) were taken directly
447 from Craig et al. [66]:

$$\frac{dN}{dt} = \left(N_{prod}^* + (\psi_N^{max} - N_{prod}^*) \frac{C_{BF} - C_{BF}^*}{C_{BF} - C_{BF}^* + \epsilon_{C,N}} \right) N_R \quad 5$$

448 Neutrophil recruitment of bone marrow reservoir neutrophils (N_R) was modelled to occur via the bound
449 fraction of G-CSF [68] ($C_{BF} = C_B(t)/(A_C N(t))$) at rate N_{prod}^* which increases towards its maximal
450 value ψ_N^{max} as a function of increasing G-CSF. During the acute phase of inflammation, endothelial
451 cells produce IL-6 leading to the attraction of neutrophils [69]. This was modelled as recruitment with
452 maximal rate $p_{N,L}$ and half-effect parameter $\epsilon_{D,L}$. Neutrophils die at rate d_N .

453 Monocytes (M) are recruited by bound GM-CSF [70], similar to neutrophils (**Eq. 5**), with bone
454 marrow monocytes (M_R) recruited at a homeostatic rate M_{prod}^* . In the presence of GM-CSF, this rate
455 increases towards ψ_M^{max} . Monocytes are also recruited by the presence of infected cells at a maximal
456 rate of $p_{M,I}$ with half-effect $\epsilon_{I,M}$, and subsequently disappear through differentiation into inflammatory
457 macrophages (as above) or death at rate d_M .

458 CD8⁺ T cells are recruited through antigen presentation on infected cells as a function of
459 infected cell numbers at rate $p_{T,I}$. The constant delay (τ_T) accounts for the time taken for dendritic cells
460 to activate, migrate to the lymph nodes, activate CD8⁺ T cells, and the arrival of effector CD8⁺ T cells
461 at the infection site. CD8⁺ T cell expansion occurs in response to bound IFN at a maximal rate $p_{T,F}$
462 with half-effect $\epsilon_{F,T}$, and CD8⁺ T-cell exhaustion occurs with high concentrations of IL-6 [16, 17], with
463 half-effect $\epsilon_{L,T}$, and apoptosis occurs at rate d_T . All variable and parameter descriptions are provided in

464 **Table S1**.

465 **Estimating early infection dynamics ('viral model')**

466 To begin estimating parameter values from data, we set all immune populations and cytokine
467 concentrations in the full model (Supplementary Information **Eqs. S1-S22**) to zero ($M_{\Phi R} = M_{\Phi I} =$
468 $M = N = T = L_U = L_B = G_U = G_B = C_U = C_B = F_U = F_B = 0$). This gives

$$\frac{dV}{dt} = pI - d_V V, \quad 6$$

$$\frac{dS}{dt} = \lambda_S \left(1 - \frac{S + I + D}{S_{max}} \right) S - \beta S V, \quad 7$$

$$\frac{dI}{dt} = \frac{\beta S(t - \tau_I)V(t - \tau_I)\epsilon_{F,I}}{\epsilon_{F,I} + F_B} - d_I I, \quad 8$$

$$\frac{dD}{dt} = d_I I - d_D D. \quad 9$$

469 We also assumed there were no resistant cells ($R = 0$) due to the absence of an IFN equation. This
 470 resulted in a simplified ‘viral model’ that considers only virus (V) infection of susceptible cells (S)
 471 which creates infected cells (I) after τ_I days, which the die through lysis, creating dead cells (D).

472 **Type I interferon dynamics during early infection (‘IFN model’)**

473 To study infection dynamics driven uniquely by IFN, we extended **Eqs. 6-9** by introducing the
 474 IFN mechanisms from **Eqs. S1-S22**, i.e. setting other cytokine and immune cell populations to zero
 475 ($M_{\Phi R} = M_{\Phi I} = M = N = T = L_U = L_B = G_U = G_B = C_U = C_B = 0$), giving

$$\frac{dV}{dt} = pI - d_V V, \quad 10$$

$$\frac{dS}{dt} = \lambda_S \left(1 - \frac{S + I + R + D}{S_{max}}\right) S - \beta S V, \quad 11$$

$$\frac{dI}{dt} = \frac{\beta S(t - \tau_I)V(t - \tau_I)\epsilon_{F,I}}{\epsilon_{F,I} + F_B} - d_I I, \quad 12$$

$$\frac{dR}{dt} = \lambda_S \left(1 - \frac{S + I + R + D}{S_{max}}\right) R + \frac{\beta S V F_B}{F_B + \epsilon_{F,I}}, \quad 13$$

$$\frac{dD}{dt} = d_I I - d_D D, \quad 14$$

$$\frac{dF_U}{dt} = \psi_F^{prod} + \frac{p_{F,I} I}{I + \eta_{F,I}} - k_{lin_F} F_U - k_{B_F} ((T^* + I)A_F - F_B) F_U + k_{U_F} F_B, \quad 15$$

$$\frac{dF_B}{dt} = -k_{int_F} F_B + k_{B_F} ((T^* + I)A_F - F_B) F_U - k_{U_F} F_B, \quad 16$$

476 where cells become resistant (R) through IFN (F_U and F_B). The parameter ψ_F^{prod} was introduced to
 477 account for the production of IFN by macrophages and monocytes not explicitly modelled in this
 478 reduced system but included in the full system (i.e. $p_{F,M}$ and $p_{F,M\Phi}$ in **Eq. S17**). Previously-fit
 479 parameters were then fixed to their estimated values (**Table S1**) and the value of ψ_F^{prod} was determined
 480 by solving $dF_U/dt = 0$ at homeostasis (i.e. $V = I = 0$), giving $\psi_F^{prod} = 0.25$.

481 **Model calibration and parameter estimation**

482 Model parameters (**Table S1**) were obtained either directly from the literature, through fitting
 483 effect curves (**Eqs. S24-S25**) or sub-models (**Eqs. S26-S56**) to *in vitro* or *in vivo* data, or by calculating

484 the value that ensured that homeostasis was maintained (**Eqs. S57-S70**) in the absence of infection. All
485 fitting procedures were performed using MATLAB 2019b functions *fmincon* or *lsqnonlin* [71].

486 Initial concentrations of all unbound cytokines ($L_{U,0}$, $G_{U,0}$, $C_{U,0}$ and $F_{U,0}$), susceptible cells,
487 resident macrophages, monocytes, neutrophils, and CD8⁺ T cells (S_0 , $M_{\Phi R,0}$, M_0 , N_0 and T_0) were
488 estimated from plasma and lung tissue concentrations in humans. Parameters for cytokine binding and
489 unbinding kinetics (**Eqs. 2-4**), such as the molecular weight (MM), binding sites per cell (K),
490 binding/unbinding rates (k_B and k_U), internalization rates for GM-CSF, G-CSF and IFN (k_{int}), and
491 cytokine clearance rates (k_{lin}), were estimated both from experimental measurements and previous
492 modelling work. The stoichiometric constants POW and \hat{p} were both equal to 1 for all cytokines,
493 except for G-CSF for which $POW = 1.4608$ and $\hat{p} = 2$ as previously estimated by Craig et al. [66].
494 Neutrophil and monocyte reservoir dynamics, monocyte differentiation, macrophage activation, and
495 CD8⁺ T cell recruitment and expansion parameters were primarily estimated from previous
496 mathematical modelling studies. Immune cell death rates were taken directly from the literature or
497 estimated from recorded half-lives using **Eq. S23**.

498 The rates of virus production, decay, infectivity, and infected cell lysis (p , d_V , β and d_I
499 respectively) were then estimated by fitting **Eqs. 6-9** to viral load measurements from SARS-CoV-2
500 infection in macaques [41] where eight adult rhesus macaques inoculated with 4×10^5 TCID₅₀/ml
501 (3×10^8 genome copies/ml) SARS-CoV-2 [41] (**Table S1**). Viral loads below 1 copy/ml were
502 assumed to be negligible. Estimated parameters for viral decay and cell lysis (d_V and d_I) were used as
503 an upper bound for parameter values in the full model.

504 A subset of parameters was obtained through fitting sigmoidal effect curves (**Eqs. S24-S25**)
505 curves to *in vitro* and *in vivo* experiments. These include the half-effect neutrophil concentration for
506 epithelial cell damage, the half-effect concentrations for monocyte production and differentiation
507 through GM-CSF signalling ($\epsilon_{G,M}$ and $\epsilon_{G,M\Phi_I}$; **Figure S1**). Other parameters obtained through effect
508 curves were the half-effects for IL-6 production by monocytes ($\eta_{L,M}$), the effect of IL-6 on monocyte
509 differentiation ($\epsilon_{L,M}$) and the half-effect of IFN on CD8⁺ T cell ($\epsilon_{F,T}$) and IL-6 on CD8⁺ T cell
510 expansion ($\epsilon_{L,T}$) (**Figure S2**).

511 These parameters were then fixed, and remaining parameters were estimated by fitting time-
512 dependent sub-models of **Eqs. S1-S22** to relevant data. The proliferation rate of epithelial cells (λ_S), the
513 internalization rate of IL-6 (k_{intL}), and the rate of neutrophil induced damage were fit to corresponding
514 time-series measurements using exponential rate terms (**Figure S2**). Clearance and phagocytosis of
515 infected cells and extracellular virus by inflammatory macrophages ($\delta_{I,M\Phi}$ and $\delta_{V,M\Phi}$) were fit to *in*

516 *vitro* experiments (**Figure S2**). Production of IFN by macrophages ($p_{F,M\Phi}$) was obtained by fitting to
517 data measuring IFN- α production (**Figure S3**). The parameters regulating the rate of the resident
518 macrophage pool replenishment ($\lambda_{M\Phi}$ and $\epsilon_{V,M\Phi}$) were estimated from *in vivo* observations of resident
519 macrophages during influenza virus infection (**Figure S3**). GM-CSF production by monocytes
520 ($p_{G,M}$; **Figure S3**), IFN production by infected cells ($p_{F,I}$), and IL-6 production by infected cells and
521 macrophages ($p_{L,I}$ and $p_{L,M\Phi}$) were all obtained from fitting reduced versions of **Eqs. S1-S22** to *in vitro*
522 experiments [47, 48, 72, 73] (**Figure S4**).

523 Lastly, any remaining parameters values were obtained by ensuring that homeostasis was
524 maintained in absence of infection (**Figure S5**). Parameters calculated from homeostasis include the
525 half-effect monocyte concentration for G-CSF production ($\eta_{C,M}$), the production rate of IL-6 and GM-
526 CSF by inflammatory macrophages ($p_{L,M\Phi}$ and $p_{G,M\Phi}$), the production rate of monocytes by GM-CSF
527 ($p_{M,G}$), and the half-effect inflammatory macrophage concentration for IFN production ($\eta_{F,M\Phi}$). For
528 some parameters it was not possible to obtain an estimation from the literature, and for these we either
529 set their value equal to an already estimated parameter ($\epsilon_{L,N}$, $p_{C,M}$, $p_{F,M\Phi}$, $\eta_{G,M\Phi}$), or qualitatively
530 estimated it ($\epsilon_{I,M}$, ρ).

531 For the ‘IFN model’ (**Eqs. 10-16**), parameters related to virus (p , d_V , β and d_I), epithelial cell
532 proliferation (λ_S and S_{max}), and IFN ($p_{F,I}$, $\eta_{F,I}$, k_{linF} , k_{BF} , A_F , k_{UF} and $\epsilon_{F,I}$) were fixed to those in **Table**
533 **S1**.

534 **Numerical simulations**

535 All ODE models were solved using *ode45* in MATLAB, and delay differentiation equations
536 (i.e. **Eqs. S1-S22**) were solved using *ddesd* in MATLAB.

537 **Sensitivity analysis**

538 We performed a local sensitivity analysis for the full model (**Eqs. S1-S22**) by individually
539 varying each parameter by $\pm 20\%$ from its estimated value and quantifying the effect on the model’s
540 output. This change was recorded and used to evaluate different metrics representing the inflammatory
541 response to SARS-CoV-2, namely maximum viral load, maximum number of dead cells, minimum
542 uninfected tissue, maximum number of inflammatory macrophages, maximum number of CD8⁺ T cells,
543 maximum unbound IL-6, maximum unbound IFN, the total exposure (AUC) to type I IFN, number of
544 days the percent of damaged tissue was $>80\%$, and time of unbound type I IFN peak. We quantified the
545 fraction of undamaged tissue by $(S + R)/S_{max}$.

546 **Virtual patient generation**

547 To generate a cohort of 200 virtual patients, we followed techniques similar to those of Allen et
 548 al. [26] and our previous studies [74, 75] wherein individual virtual patients were created by sampling a
 549 parameter set \mathbf{p} from parameter distributions then simulating the model to verify that each individual's
 550 trajectory was realistic. A subset of parameters ($p_{M\Phi,I,L}$, $p_{L,M\Phi}$, $p_{F,I}$, $p_{M,I}$, $\eta_{F,M\Phi}$, $\epsilon_{F,I}$, and $p_{F,M}$) was
 551 designated as patient-specific after considering the results of the sensitivity analysis and standard
 552 deviations inferred from clinical observations (Supplementary Information). To avoid the inclusion of
 553 unrealistic dynamics, patient parameter sets were then optimized using simulated annealing to ensure
 554 predictions fell within physiological ranges for viral load [41], IL-6 [6, 44], IFN- α [42], and G-CSF
 555 [24] (**Figure 7**).

556 The upper u_i and lower l_i bounds for V , L_U , F_U and C_U were based off these physiological
 557 ranges from Munster et al. [41] (viral loads), Herold et al. [44] (IL-6 concentrations), Trouillet-Assant
 558 et al. [42] (IFN dynamics), and Liu et al. [7] (G-CSF concentrations) as described in Supplementary
 559 Information Section S.6.1. Intervals for each patient-specific parameter set were restricted to four
 560 standard deviations from the mean or zero if the lower bound was negative. Given an initial patient
 561 specific parameter set \mathbf{p} , we used simulated annealing to minimize $J(\mathbf{p})$, i.e.

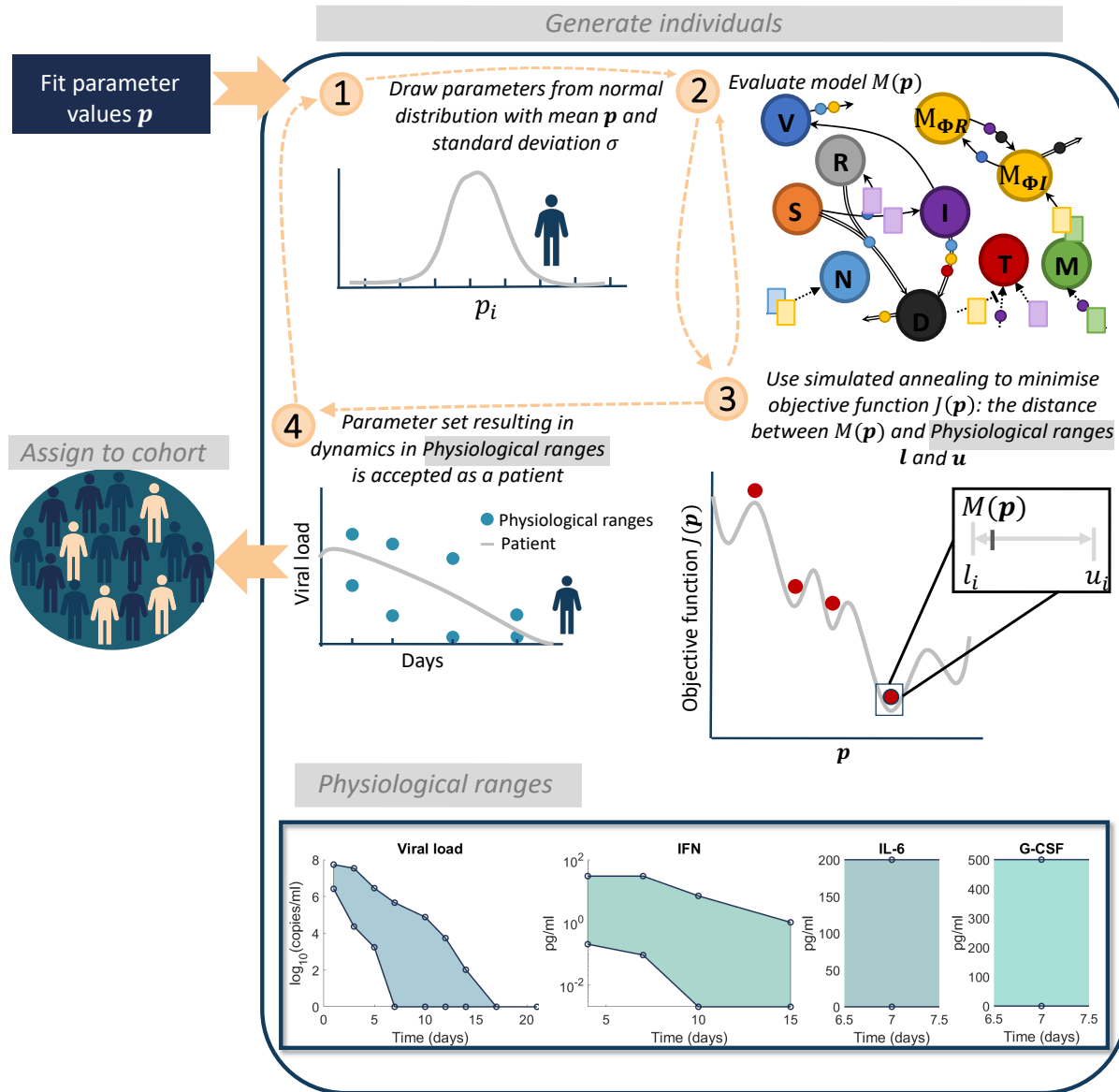
$$\min_{\mathbf{p}} J(\mathbf{p}) = \min_{\mathbf{p}} \left[\sum_i \max \left(\left(M_i(\mathbf{p}) - \frac{l_i + u_i}{2} \right)^2 - \left(u_i - \frac{l_i + u_i}{2} \right)^2, 0 \right) \right], \quad 17$$

562 where $M_i(\mathbf{p})$ is the model output i evaluated at parameter set \mathbf{p} corresponding to the upper and lower
 563 bound l_i and u_i (**Figure 7**).

564 To quantify disease severity for each patient, we introduced an inflammation variable (Ψ) to
 565 account for the combined changes in IL-6 (L_U), neutrophils (N), and damaged tissue ($S + R$), each
 566 normalized by the virtual cohort's average. In this way, Ψ measures an individual's relative change
 567 from the cohort's baseline, and quantifies the contributions of IL-6, neutrophils, and tissue damage on
 568 comparable scales. For a given patient j , the inflammation marker is given by

$$\Psi^j = \frac{\max_t(L_U^j(t))}{\frac{1}{n} \sum_{j=1}^n \left(\max_t(L_U^j(t)) \right)} + \frac{\max_t(N^j(t))}{\frac{1}{n} \sum_{j=1}^n \left(\max_t(N^j(t)) \right)} + \frac{S_{max} - \min_t(S^j(t) + R^j(t))}{\frac{1}{n} \sum_{j=1}^n \left(S_{max} - \min_t(S^j(t) + R^j(t)) \right)}, \quad 18$$

569 where n is the total number of patients in the cohort, and L_U^j , N^j , S^j , and R^j are the unbound IL-6,
 570 neutrophils, and susceptible and resistant epithelial cell count, respectively.



571

572 **Figure 7. Algorithm for generating virtual patients.** Parameters in the model were first obtained through
 573 fitting to data (Table S1). **1**) Parameters relating to macrophage, IL-6 and IFN production
 574 ($p_{M\Phi,L}$, $p_{L,M\Phi}$, $p_{F,I}$, $p_{M,I}$, $\eta_{F,M\Phi}$, $\epsilon_{F,I}$, and $p_{F,M}$) were generated from normal distributions with mean equal to
 575 their original fitted values and standard deviation informed by experiment observations (see Section S6.1). **2)**
 576 The model evaluated is then evaluated on this parameter set to obtain $y(t, p)$. **3)** A simulated annealing
 577 algorithm is then used to determine a parameter set that optimises the objective function $J(p)$ (Eq.16). **4)**
 578 Optimizing the objective function provides a parameter set for which the patient response to SARS-CoV-2 will
 579 be within the physiological ranges. This patient is then assigned to the cohort and this process is continued until
 580 200 patients have been generated. Physiological ranges are noted in the bottom box for viral load [41], IFN [42],
 581 IL-6 [44] and G-CSF [7].

582 Statistical analyses

583 The Pearson correlation coefficient (R) was used to measure the degree of interaction between two
 584 variables, with a significance level of $\alpha < 0.05$ indicating rejection of the hypothesis that there is no
 585 relationship between the observed variables. In addition, we used two-sample two-sided t-tests (number

586 of patients < 40) and z-tests (number of patients ≥ 40) at the $\alpha < 0.05$ significance level to test the
587 hypothesis that there were no differences between sample means.

588 **Acknowledgments**

589 All authors would like to thank Paul Macklin and Thomas Hillen for encouraging collaboration.

590 **Funding**

591 ALJ was supported by Fonds de recherche Santé Québec Programme de bourse de formation
592 postdoctorale pour les citoyens d'autres pays and a Centre for Applied Mathematics in Bioscience and
593 Medicine (CAMBAM) Postdoctoral fellowship. RA and AMS were supported by NIH R01 AI139088.
594 ALJ and MC were supported by NSERC Discovery Grant RGPIN-2018-04546 and NSERC Alliance
595 COVID-19 ALLRP 554923 – 20.

596 **Author contributions**

597 ALJ, RA, AMS, CLD, and MC conceived the study. AMS and APS conducted the alveolar
598 macrophage and viral load *in vivo* experiments. PAM contributed significant immunological insight.
599 All authors contributed intellectual insight into the development of the study. ALJ and MC wrote the
600 code and manuscript with significant contributions from all authors.

601 **Competing interests**

602 The authors declare no competing interests.

603 **Data and materials availability**

604 All data needed to evaluate the conclusions in the paper are present in the paper and/or the
605 Supplementary Materials.”). Sample code is available upon reasonable request to the corresponding
606 author.

607 **References**

- 608 1. Mehta P, McAuley DF, Brown M, Sanchez E, Tattersall RS, Manson JJ. COVID-19: consider
609 cytokine storm syndromes and immunosuppression. *Lancet*. 2020;395(10229):1033-1034.
610 doi:[https://doi.org/10.1016/S0140-6736\(20\)30628-0](https://doi.org/10.1016/S0140-6736(20)30628-0)
- 611 2. Zhou P, Yang X-L, Wang X-G, et al. A pneumonia outbreak associated with a new coronavirus
612 of probable bat origin. *Nature*. 2020;579(7798):270-273. doi:10.1038/s41586-020-2012-7
- 613 3. Qin C, Zhou L, Hu Z, et al. Dysregulation of immune response in patients with COVID-19 in
614 Wuhan, China. *Prepr with Lancet*. 2020;February 1:1-18.
- 615 4. Wu F, Zhao S, Yu B, et al. A new coronavirus associated with human respiratory disease in
616 China. *Nature*. 2020;579(7798):265-269. doi:10.1038/s41586-020-2008-3
- 617 5. Stebbing J, Phelan A, Griffin I, et al. COVID-19: combining antiviral and anti-inflammatory
618 treatments. *Lancet Infect Dis*. 2020;20(4):400-402. doi:[https://doi.org/10.1016/S1473-](https://doi.org/10.1016/S1473-3099(20)30132-8)
619 [3099\(20\)30132-8](https://doi.org/10.1016/S1473-3099(20)30132-8)
- 620 6. Lucas C, Wong P, Klein J, et al. Longitudinal analyses reveal immunological misfiring in severe
621 COVID-19. *Nature*. 2020:1-9.
- 622 7. Liu J, Li S, Liu J, et al. Longitudinal characteristics of lymphocyte responses and cytokine
623 profiles in the peripheral blood of SARS-CoV-2 infected patients. *EBioMedicine*. 2020:102763.
- 624 8. Duployez N, Demonchy J, Berthon C, et al. Clinico-biological features and clonal hematopoiesis
625 in patients with severe covid-19. *Cancers (Basel)*. 2020;12(7):1-11.
626 doi:10.3390/cancers12071992
- 627 9. Nathan C. Neutrophils and COVID-19: Nots, NETs, and knots. *J Exp Med*.
628 2020;217(9):e20201439.
- 629 10. Jamilloux Y, Henry T, Belot A, et al. Should we stimulate or suppress immune responses in

- 630 COVID-19? Cytokine and anti-cytokine interventions. *Autoimmun Rev.* 2020:102567.
631 doi:10.1016/j.autrev.2020.102567
- 632 11. Mathew D, Giles JR, Baxter AE, et al. Deep immune profiling of COVID-19 patients reveals
633 distinct immunotypes with therapeutic implications. *Science (80-)*.
634 2020;1209(September):eabc8511. doi:10.1126/science.abc8511
- 635 12. Blanco-Melo D, Nilsson-Payant BE, Liu W-C, et al. Imbalanced host response to SARS-CoV-2
636 drives development of COVID-19. *Cell.* 2020;181(5):1036-1045.e9.
- 637 13. Channappanavar R, Fehr AR, Zheng J, et al. IFN-I response timing relative to virus replication
638 determines MERS coronavirus infection outcomes. *J Clin Invest.* 2019;129(9):3625-3639.
639 doi:10.1172/JCI126363
- 640 14. Channappanavar R, Fehr AR, Vijay R, et al. Dysregulated type I interferon and inflammatory
641 monocyte-macrophage responses cause lethal pneumonia in SARS-CoV-infected mice. *Cell*
642 *Host Microbe.* 2016;19(2):181-193. doi:https://doi.org/10.1016/j.chom.2016.01.007
- 643 15. Li B, Jones LL, Geiger TL. IL-6 promotes T cell proliferation and expansion under
644 inflammatory conditions in association with low-level ROR γ t expression. *J Immunol.*
645 2018;201(10):2934-2946.
- 646 16. Liu T, Zhang J, Yang Y, et al. The role of interleukin-6 in monitoring severe case of coronavirus
647 disease 2019. *EMBO Mol Med.* 2020.
- 648 17. Laing AG, Lorenc A, del Molino del Barrio I, et al. A dynamic COVID-19 immune signature
649 includes associations with poor prognosis. *Nat Med.* 2020. doi:10.1038/s41591-020-1038-6
- 650 18. Bastard P, Rosen LB, Zhang Q, et al. Auto-antibodies against type I IFNs in patients with life-
651 threatening COVID-19. *Science (80-)*. 2020;4585:eabd4585. doi:10.1126/science.abd4585
- 652 19. Seo Y-J, Hahm B. Type I interferon modulates the battle of host immune system against viruses.
653 *Adv Appl Microbiol.* 2010;73:83-101. doi:10.1016/S0065-2164(10)73004-5
- 654 20. Arnaud P. The interferons: pharmacology, mechanism of action, tolerance and side effects. *La*
655 *Rev Med interne.* 2002;23:449s-458s.
- 656 21. Smith AM, Perelson AS. Influenza A virus infection kinetics: quantitative data and models.
657 *Wiley Interdiscip Rev Syst Biol Med.* 2011;3(4):429-445. doi:10.1002/wsbm.129
- 658 22. Jamilloux Y, Henry T, Belot A, et al. Should we stimulate or suppress immune responses in
659 COVID-19? Cytokine and anti-cytokine interventions. *Autoimmun Rev.* 2020.
- 660 23. Widagdo W, Okba NMA, Stalin Raj V, Haagmans BL. MERS-coronavirus: From discovery to
661 intervention. *One Heal.* 2017;3:11-16. doi:https://doi.org/10.1016/j.onehlt.2016.12.001
- 662 24. Long Q-X, Tang X-J, Shi Q-L, et al. Clinical and immunological assessment of asymptomatic
663 SARS-CoV-2 infections. *Nat Med.* 2020:1-5.
- 664 25. Jenner AL, Aogo RA, Davis CL, Smith AM, Craig M. Leveraging Computational Modelling to
665 Understand Infectious Diseases. *Curr Pathobiol Rep.* 2020;In press.
- 666 26. Allen RJ, Rieger TR, Musante CJ. Efficient Generation and Selection of Virtual Populations in
667 Quantitative Systems Pharmacology Models. *CPT Pharmacometrics Syst Pharmacol.*
668 2016;5(3):140-146. doi:10.1002/psp4.12063
- 669 27. Cassidy T, Humphries AR, Craig M, Mackey MC. Characterizing chemotherapy-induced
670 neutropenia and monocytopenia through mathematical modelling. *bioRxiv.*
671 2020:2020.04.02.022046. doi:10.1101/2020.04.02.022046
- 672 28. Alfonso S, Jenner AL, Craig M. Translational approaches to treating dynamical diseases through
673 in silico clinical trials. *Chaos An Interdiscip J Nonlinear Sci.* 2020;In review.
- 674 29. Smith AM. Host-pathogen kinetics during influenza infection and coinfection: insights from
675 predictive modeling. *Immunol Rev.* 2018;285(1):97-112.
- 676 30. Jenner AL, Yun C-O, Yoon A, Coster ACF, Kim PS. Modelling combined virotherapy and
677 immunotherapy: strengthening the antitumour immune response mediated by IL-12 and GM-
678 CSF expression. *Lett Biomath.* 2018;5(sup1). doi:10.1080/23737867.2018.1438216

- 679 31. Goyal A, Cardozo-Ojeda EF, Schiffer JT. Potency and timing of antiviral therapy as
680 determinants of duration of SARS CoV-2 shedding and intensity of inflammatory response.
681 *medRxiv*. 2020:2020.04.10.20061325. doi:10.1101/2020.04.10.20061325
- 682 32. Waghmare A, Krantz EM, Baral S, et al. Reliability of self-sampling for accurate assessment of
683 respiratory virus viral and immunologic kinetics. *medRxiv*. January 2020:2020.04.03.20051706.
684 doi:10.1101/2020.04.03.20051706
- 685 33. Kim KS, Ejima K, Ito Y, et al. Modelling SARS-CoV-2 dynamics: implications for therapy.
686 *medRxiv*. January 2020:2020.03.23.20040493. doi:10.1101/2020.03.23.20040493
- 687 34. Ejima K, Kim KS, Ito Y, et al. Inferring timing of infection using within-host SARS-CoV-2
688 infection dynamics model: Are “imported cases” truly imported? *medRxiv*. January
689 2020:2020.03.30.20040519. doi:10.1101/2020.03.30.20040519
- 690 35. Sahoo S, Hari K, Jhunjhunwala S, Jolly MK. Mechanistic modeling of the SARS-CoV-2 and
691 immune system interplay unravels design principles for diverse clinicopathological outcomes.
692 *bioRxiv*. January 2020:2020.05.16.097238. doi:10.1101/2020.05.16.097238
- 693 36. Sego T, Aponte-Serrano JO, Gianlupi JF, et al. A modular framework for multiscale
694 multicellular spatial modeling of viral infection, immune response and drug therapy timing and
695 efficacy in epithelial tissues: A multiscale model of viral infection in epithelial tissues. *BioRxiv*.
696 2020.
- 697 37. Sadler AJ, Williams BRG. Interferon-inducible antiviral effectors. *Nat Rev Immunol*.
698 2008;8(7):559-568.
- 699 38. Chomarat P, Banchereau J, Davoust J, Karolina Palucka A. IL-6 switches the differentiation of
700 monocytes from dendritic cells to macrophages. *Nat Immunol*. 2000;1(6):510-514.
701 doi:10.1038/82763
- 702 39. Drescher, Brandon and Bai F. Neutrophil in viral infections, friend or foe? *Virus Res*.
703 2013;171(1):1-7.
- 704 40. Galani IE, Andreacos E. Neutrophils in viral infections: current concepts and caveats. *J Leukoc*
705 *Biol*. 2015;98(4):557-564. doi:10.1189/jlb.4VMR1114-555R
- 706 41. Munster VJ, Feldmann F, Williamson BN, et al. Respiratory disease in rhesus macaques
707 inoculated with SARS-CoV-2. *Nature*. 2020. doi:10.1038/s41586-020-2324-7
- 708 42. Trouillet-Assant S, Viel S, Gaymard A, et al. Type I IFN immunoprofiling in COVID-19
709 patients. *J Allergy Clin Immunol*. 2020:4-8. doi:10.1016/j.jaci.2020.04.029
- 710 43. Zhao Y, Qin L, Zhang P, et al. Longitudinal COVID-19 profiling associates IL-1Ra and IL-10
711 with disease severity and RANTES with mild disease. *JCI Insight*. 2020;5(13).
712 doi:10.1172/jci.insight.139834
- 713 44. Herold T, Jurinovic V, Arnreich C, et al. Elevated levels of interleukin-6 and CRP predict the
714 need for mechanical ventilation in COVID-19. *J Allergy Clin Immunol*. 2020.
- 715 45. Sheahan TP, Sims AC, Leist SR, et al. Comparative therapeutic efficacy of remdesivir and
716 combination lopinavir, ritonavir, and interferon beta against MERS-CoV. *Nat Commun*.
717 2020;11(1):222. doi:10.1038/s41467-019-13940-6
- 718 46. Kratochvil RM, Kubes P, Deniset JF. Monocyte conversion during inflammation and injury.
719 *Arterioscler Thromb Vasc Biol*. 2017;37(1):35-42.
- 720 47. Shibata Y, Berclaz P-Y, Chroneos ZC, Yoshida M, Whitsett JA, Trapnell BC. GM-CSF
721 Regulates Alveolar Macrophage Differentiation and Innate Immunity in the Lung through PU.1.
722 *Immunity*. 2001;15(4):557-567. doi:10.1016/S1074-7613(01)00218-7
- 723 48. Ioannidis I, Ye F, McNally B, Willette M, Flaño E. Toll-Like Receptor Expression and
724 Induction of Type I and Type III Interferons in Primary Airway Epithelial Cells. *J Virol*.
725 2013;87(6):3261. doi:10.1128/JVI.01956-12
- 726 49. Pawelek KA, Dor Jr D, Salmeron C, Handel A. Within-host models of high and low pathogenic
727 influenza virus infections: The role of macrophages. *PLoS One*. 2016;11(2):2016.

- 728 50. Eftimie R, Eftimie G. Tumour-associated macrophages and oncolytic virotherapies: a
729 mathematical investigation into a complex dynamics. *Lett Biomath.* 2018;5(sup1):S6-S35.
730 doi:10.1080/23737867.2018.1430518
- 731 51. Patel AA, Zhang Y, Fullerton JN, et al. The fate and lifespan of human monocyte subsets in
732 steady state and systemic inflammation. *J Exp Med.* 2017;214(7):1913-1923.
- 733 52. Krummel MF, Mahale JN, Uhl LF, et al. Paracrine costimulation of IFN- γ signaling by
734 integrins modulates CD8 T cell differentiation. *Proc Natl Acad Sci.* 2018;115(45):11585-11590.
- 735 53. Ohta M, Okabe T, Ozawa K, Urabe A, Takaku F. $1\alpha,25$ -Dihydroxy vitamin D₃ (calcitriol)
736 stimulates proliferation of human circulating monocytes in vitro. *FEBS Lett.* 1985;185(1):9-13.
737 doi:10.1016/0014-5793(85)80730-4
- 738 54. Krilov LR, Hendry RM, Godfrey E, McIntosh K. Respiratory Virus Infection of Peripheral
739 Blood Monocytes: Correlation with Ageing of Cells and Interferon Production in vitro. *J Gen
740 Virol.* 1987;68(6):1749-1753. doi:<https://doi.org/10.1099/0022-1317-68-6-1749>
- 741 55. Goudot C, Coillard A, Villani A-C, et al. Aryl hydrocarbon receptor controls monocyte
742 differentiation into dendritic cells versus macrophages. *Immunity.* 2017;47(3):582-596.
- 743 56. Desalegn G, Pabst O. Inflammation triggers immediate rather than progressive changes in
744 monocyte differentiation in the small intestine. *Nat Commun.* 2019;10(1):1-14.
- 745 57. Karki R, Raj B, Tuladher, S et al. COVID-19 cytokines and the hyperactive immune response:
746 Synergism of TNF- α and IFN- γ in triggering inflammation, tissue damage, and death. *bioRxiv.*
747 2020:2020.10.29.361048.
- 748 58. Della-Torre E, Campochiaro C, Cavalli G, et al. Interleukin-6 blockade with sarilumab in severe
749 COVID-19 pneumonia with systemic hyperinflammation: an open-label cohort study. *Ann
750 Rheum Dis.* 2020;79(10):1277-1285.
- 751 59. Santillán M. On the use of the Hill functions in mathematical models of gene regulatory
752 networks. *Math Model Nat Phenom.* 2008;3(2):85-97.
- 753 60. Janeway C. *Immunobiology 5: The Immune System in Health and Disease.* New York: Garland
754 Pub.; 2001.
- 755 61. Louten J. Virus Transmission and Epidemiology. In: *Essential Human Virology.* Elsevier;
756 2016:71-92. doi:10.1016/b978-0-12-800947-5.00005-3
- 757 62. Nagarajan UM. Induction and function of IFN β during viral and bacterial infection. *Crit Rev
758 Immunol.* 2011;31(6):459-474. doi:10.1615/critrevimmunol.v31.i6.20
- 759 63. Arnaud P. Different interferons: Pharmacology, pharmacokinetics, proposed mechanisms, safety
760 and side effects. *Rev Med Interne.* 2002;23(SUPPL. 4):449S-458S. doi:10.1016/S0248-
761 8663(02)00659-8
- 762 64. Elmore S. Apoptosis: a review of programmed cell death. *Toxicol Pathol.* 2007;35(4):495-516.
763 doi:10.1080/01926230701320337
- 764 65. Klöditz K, Fadeel B. Three cell deaths and a funeral: macrophage clearance of cells undergoing
765 distinct modes of cell death. *Cell death Discov.* 2019;5(1):1-9.
- 766 66. Craig M, Humphries AR, Mackey MC. A Mathematical Model of Granulopoiesis Incorporating
767 the Negative Feedback Dynamics and Kinetics of G-CSF/Neutrophil Binding and
768 Internalization. *Bull Math Biol.* 2016;78(12):2304-2357. doi:10.1007/s11538-016-0179-8
- 769 67. Shi Y, Liu CH, Roberts AI, et al. Granulocyte-macrophage colony-stimulating factor (GM-CSF)
770 and T-cell responses: what we do and don't know. *Cell Res.* 2006;16(2):126-133.
- 771 68. Takei Y, Ando H, Tsutsui K, eds. About the Editors. In: *Handbook of Hormones.* San Diego:
772 Academic Press; 2016:v. doi:<https://doi.org/10.1016/B978-0-12-801028-0.00292-0>
- 773 69. Scheller J, Chalaris A, Schmidt-Arras D, Rose-John S. The pro-and anti-inflammatory properties
774 of the cytokine interleukin-6. *Biochim Biophys Acta (BBA)-Molecular Cell Res.*
775 2011;1813(5):878-888.
- 776 70. Rösler B, Herold S. Lung epithelial GM-CSF improves host defense function and epithelial

- 777 repair in influenza virus pneumonia—a new therapeutic strategy? *Mol Cell Pediatr.*
778 2016;3(1):29. doi:10.1186/s40348-016-0055-5
- 779 71. Matlab 2019a. 2019.
- 780 72. Lee M-T, Kaushansky K, Ralph P, Ladner MB. Differential Expression of M-CSF, G-CSF, and
781 GM-CSF by Human Monocytes. *J Leukoc Biol.* 1990;47(3):275-282. doi:10.1002/jlb.47.3.275
- 782 73. Ye S, Lowther S, Stambas J. Inhibition of reactive oxygen species production ameliorates
783 inflammation induced by influenza A viruses via upregulation of SOCS1 and SOCS3. *J Virol.*
784 2015;89(5):2672-2683.
- 785 74. Jenner AL, Cassidy T, Belaid K, Bourgeois-Daigneault M-C, Craig M. In silico trials predict
786 that combination strategies for enhancing vesicular stomatitis oncolytic virus are determined by
787 tumour aggressivity. *J Immunother Cancer.* 2020;In review.
- 788 75. Cassidy T, Craig M. Determinants of combination GM-CSF immunotherapy and oncolytic
789 virotherapy success identified through in silico treatment personalization. Goldman A, ed. *PLOS*
790 *Comput Biol.* 2019;15(11):e1007495. doi:10.1371/journal.pcbi.1007495
- 791

792 Supporting information captions

793

794 Supplementary Information file.

795 **Figure S1. Effects of neutrophils on lung epithelial cells, GM-CSF on monocyte production and**
796 **differentiation, the relationships between monocytes and CD4+ T cells with IL-6, and the**
797 **influence of IFN on T cell expansion. A)** Using the measurements by Knaapen et al.²², the
798 inhibitory effect curve E (Eq. S25) was fit to the cell viability of RLE cells under various
799 concentrations of H₂O₂. **B)** The stimulatory effect curve E (Eq. S24) was fit to the dose response
800 measurements of blood monoculture cells (3×10^3 cells/dish) with various concentrations of
801 murine recombinant GM-CSF (IU/ml)¹⁸. **C)** The stimulatory effect curve E (Eq. S24) was fit to
802 measurements for the monocytic myeloid cell count as a function of GM-CSF.¹⁷ **D)** Eq. S27 fit
803 to time course data of IL-6 production from monocytes³⁸. **E)** IL-6 stimulation of monocyte
804 differentiation to macrophages modelled by the inhibitory effect curve E (Eq. S24) fit to the
805 percentage of CD14+ cells (macrophages) as a function of the number of fibroblasts measured
806 by Chomarat et al.¹⁶. **F)** Stimulatory effect curve E (Eq. S24) for IFN- γ stimulation on CD8+ T
807 cells fit to measurements of the signalling in CD8+T cells for varying doses of IFN- γ ¹⁹. Data
808 (black) is plotted as either circles (**D & E**) or mean and standard deviation error bars (**A-C&F**);
809 solid blue line: corresponding fit.

810 **Figure S2. Dynamics of IL-6 on T cell expansion, epithelial cell growth, IL-6 internalization,**
811 **neutrophil-induced damage, and macrophage phagocytosis. A)** Effect curve (Eq. S24) for
812 the IL-6 effect on T cell expansion fit to measurements CD4+ T cells from dilutions of IL-6 by
813 Holsti and Raulet²¹. **B)** Exponential growth curve fit to the growth of A549 cells² **C)** The
814 internalization rate of IL-6 (Eq. S30) fit to the fraction of internalized IL-6⁴⁷. **D)** Exponential
815 decay fit to cell viability after H₂O₂ administration²⁴. **E)** The macrophage clearance of apoptotic
816 material (Eqs. S31-S33) was fit to the percentage of macrophages that had engulfed material
817 over 25 hours²⁷. **F)** The phagocytosis rate of extracellular virus by macrophages was obtained by
818 fitting Eqs. S34-S35 to the uptake of virus by macrophages measured by Rigden et al.²³. Data
819 (black) is plotted as either circles (**A & F**) or mean and standard deviation error bars (**B-E**); solid
820 blue line: corresponding fit.

821 **Figure S3. Monocyte expansion and type I IFN production by monocytes, alveolar macrophage**
822 **replenishment after viral infection, and GM-CSF production by monocytes. A)** Eq. S37 fit
823 to time course of proliferation of monocytes in culture⁴². **B)** Fit of Eqs. S38-S39 to the
824 production of IFN- α by monocytes after 24 hours with RSV as a function of the number of days

825 of pre-culturing (1, 2, 4 or 7)⁴³. **C**) Correlation between infectious virus titre and RT-PCR copy
826 number for influenza A and B measured by Laurie et al.⁸⁸ The relative TCID₅₀ compared to the
827 RNA copies is plotted for each virus strain and the mean as a black dashed line. **D-E**) Fit of **Eqs.**
828 **S40-S42** to viral loads⁸⁷ and alveolar macrophages from experimental influenza infections. **F**)
829 The production of GM-CSF from stimulated monocytes was recorded by Lee et al.⁴⁰ Using a
830 simplified version of the full model (**Eqs. S43-S46**), we obtained the production rates for
831 monocytes and GM-CSF. Data (black) is plotted as either circles/stars (**B&F**) or mean and
832 standard deviation error bars (**A,D-E**); solid blue line: corresponding fit.

833 **Figure S4. Production of IFN and IL-6 by infected cells and macrophages.** **A**) Concentration of
834 IFN- β released by alveolar epithelial cells in response to stimulation with influenza virus
835 recorded at 8, 16 and 24 hours⁴¹. **B-C**) IL-6 production by infected cells in response to **A**) H5NA
836 and **B**) H7N9, measured by Ye et al.³⁶ Data (black) is plotted as mean and standard deviation
837 error bars with the corresponding fit (**Eqs. S51-S54**) in solid blue. **D**) IL-6 production by
838 macrophages (**Eq. S56**) in response to stimulation with LPS of varying dosage sizes. Shibata et
839 al.³⁷ measured the production of IL-6 for different dosages of LPS and fitting the production
840 rate to this data to obtain $p_{L,M\Phi}, \eta_{L,M\Phi}$.

841 **Figure S5. Homeostatic disease-free system regulation.** **A**) To confirm that parameters in the model
842 represented realistic immunocompetent individuals in the disease-free scenario, **Eqs. S1-S22**
843 were simulated where $V_0 = 0$ and parameters were given by the homeostasis **Eqs. S57-S70**. The
844 initial concentration of G-CSF was perturbed and compared to simulations of the model at
845 homeostasis. Simulations at homeostasis are represented by solid lines (purple) and perturbed
846 simulations as dashed lines (pink). **B**) The maximum residual between variables and their initial
847 conditions at day 50 was measured to confirm that the system was stable for perturbations in all
848 immune cells and cytokines.

849 **Figure S6. Model validation against human cytokine measurements during SARS-CoV-2**
850 **infection.** **A**) IFN dynamics of the reduced model (**Figure 3 Main Text**) overlaid with patient
851 IFN- $\alpha 2$ plasma concentrations from Trouillet-Assant et al.⁷⁰ The solid line (purple) represents
852 the unbound IFN dynamics from the reduced model (**Eqs. 27-33**). Individual patient IFN- $\alpha 2$
853 measurements are plotted as grey circles. Normal IFN- $\alpha 2$ concentration in healthy volunteers
854 are indicated by a grey area. **B-F**) Mild and severe dynamics (**Eqs. S1-S22**) corresponding to
855 simulations in **Figure 4 Main Text** and **Figure S7** overlaid with measurements from the
856 literature with solid lines: mild disease dynamics; dashed lines: severe disease dynamics. **B-C**)
857 Plasma IFN- α and IL-6 in COVID-19 critically ill patients (n=26) obtained by Trouillet-Assant
858 et al.⁷⁰ overlaid with mild and severe unbound IFN ($F_U(t)$) and mild and severe unbound IL-6
859 ($L_U(t)$). **D**) IL-6 levels in patients requiring and not requiring mechanical ventilation obtained
860 by Herold et al.⁹¹ overlaid with mild and severe unbound IL-6 dynamics. **E-F**) IL-6 and G-CSF
861 plasma concentration obtained by Long et al.⁹² in symptomatic “S” and asymptomatic “AS”
862 COVID-19 patients overlaid with corresponding mild and severe model dynamics.

863 **Figure S7. Predicting mild and severe COVID-19 dynamics (all model variables).** Extension of
864 results of mild and severe disease dynamics in **Figure 4 Main Text**. Mild disease (solid lines)
865 dynamics obtained by using baseline parameter estimates (**Tables S1**) while severe disease
866 dynamics (dashed lines) were obtained by decreasing the production rate of type I IFN, $p_{F,I}$, and
867 increasing the production of monocytes, $p_{M,I}$, and their differentiation to macrophages, $\eta_{F,M\Phi}$.
868 **A**) Lung cells concentrations (susceptible cells $S(t)$, resistant cells $R(t)$, infected cells $I(t)$, dead
869 cells $D(t)$ and virus $V(t)$). Solid black line with error bars indicates macaque data (see **Fig. 2**
870 **Main Text**). **B**) Immune cell concentrations (resident macrophages $M_{\Phi R}(t)$, inflammatory
871 macrophages $M_{\Phi I}(t)$, monocytes $M(t)$, neutrophils $N(t)$ and T cells $T(t)$). **C**) Bound and
872 unbound cytokine concentrations (IL-6 unbound $L_U(t)$ and bound $L_B(t)$, GM-CSF unbound

873 $G_U(t)$ and bound $G_B(t)$, G-CSF unbound $C_U(t)$ and bound $C_B(t)$, type I IFN unbound $F_U(t)$ and
874 bound $F_B(t)$).

875 **Figure S8. Full analysis of parameters driving COVID-19 severity.** A local sensitivity analysis was
876 performed by varying each parameter $\pm 20\%$ from its originally estimated value and simulating
877 the model. Predictions were then compared to baseline considering: Maximum viral load
878 ($\max(V)$), maximum concentration of dead cells ($\max(D)$), minimum uninfected live cells
879 ($\min(S+R)$), maximum concentration of inflammatory macrophages ($\max(M_{\phi I})$), maximum
880 number of CD8⁺ T cells ($\max(T)$), maximum concentration of IL-6 ($\max(L_U)$), maximum
881 concentration of type I IFN ($\max(F_U)$), the total exposure to type I IFN (F_U exposure), the
882 number of days damaged tissue was $>80\%$ ($\text{time}(S+R)/S_{max} < 0.2$), and the day type I IFN
883 reached its maximum (day $\max(F_U)$). The heatmaps show the fold change of each metric, where
884 blue signifies the minimum value observed and red signifies the maximum value observed, or by
885 the number of days, where light to dark pink signifying increasing number of days from zero.
886 The most sensitive parameters are shown in **Figure 5** in the **Main Text**.

887 **Figure S9. Cohort dynamics within physiological ranges.** Virtual patients were generated so that
888 viral load, IFN and IL-6 concentration were within physiological ranges obtained in the
889 literature. The physiological ranges (denoted by open circles) were obtained from **A**) Munster et
890 al.⁹⁶, **B**) Trouillet-Assant et al.⁷⁰, and **C**) Herold et al.⁹¹. Patient dynamics at discrete time points
891 are plotted as joined green dots.

892 **Table S1. Parameter values used in the Main Text.** Parameters have been grouped into: (a-e) cell
893 related, (f-k) cytokine related parameters (l) and initial conditions. Relevant references are given
894 estimated parameters. Parameters obtained through fitting to data in the literature have the
895 appropriate figure noted in the Info column. Parameters estimated from homeostasis calculation
896 are denoted by H or qualitatively estimated by E. Parameters whose value was taken from
897 another parameters estimated has that parameter noted. Viral load is reported as virion copies
898 and cells have been noted in 10^9 cells. Time t is in days. The final sub-table (m) is a list of the
899 variables in the model.